The Life Cycle of TTL Cirrus: A Model Evaluation using the DYAMOND Simulations

Samantha M. Turbeville

A thesis
submitted in partial fulfillment of the
requirements for the degree of

Master of Science

University of Washington

2021

Committee:

Thomas Ackerman

Christopher Bretherton

Peter Blossey

Qiang Fu

Program Authorized to Offer Degree:
Department of Atmospheric Sciences

University of Washington

Abstract

The Life Cycle of TTL Cirrus: A Model Evaluation using the DYAMOND Simulations

Samantha M. Turbeville

Chair of the Supervisory Committee:

Thin cirrus in the tropics are important for climate because of their warming effect on the atmosphere and large spatiotemporal extent, coinciding with locations of deep convection. Tropical cirrus are difficult to observe due to their high altitude and thin optical depths. They are also difficult to simulate in conventional global climate models because of the coarse grid spacing and simplified parameterizations of deep convection and cirrus formation in such models. We investigate the representation of tropical cirrus in global storm-resolving models (GSRMs) because they have higher spatiotemporal resolution and explicit convection, which could provide a more accurate representation of cloud processes. This study uses GSRMs from the DYnamics of the Atmospheric general circulation Modeled On Non-hydrostatic Domains (DYAMOND) project. The aggregate life cycle of topical cirrus are analyzed using joint albedo-OLR histograms to determine the fidelity of models in capturing the observed distribution of cloud populations over representative tropical ocean and land regions. Some models generate more optically thick cirrus or anvils while thin cirrus dominate in other models. Model differences, likely driven by sub-grid processes such as ice microphysics, dominate over the more subtle regional shifts. Understanding the differences in the GSRMs is an important step toward reducing uncertainty in predictions of future warming that is generated by high cloud feedbacks.

TABLE OF CONTENTS

LIST OF FIGURES

Chapter 1

INTRODUCTION

High clouds in the tropics have historically been difficult to accurately reproduce in numerical simulations because of their complex microphysics and radiative properties (e.g., Del Genio, 2012; Stephens, 2005). Proper representation of the properties of tropical cirrus, especially cloud amount and hydrometeor distribution, is a key issue for improving global climate models (GCMs) (Inoue et al., 2010). GCMs generally have a low spatiotemporal resolution, which is unable to accurately represent convection and the subsequent tropical cloud life cycles. Due to the different convective parameterizations, there can be large differences between GCMs, especially in the ice clouds (Del Genio, 2012). In addition, ice microphysics is not well-represented in models due to the complexity of ice property evolution.

One difficulty of computing ice properties is the lack of understanding of ice cloud properties in the present atmosphere. Active satellite sensors have large uncertainties with thin cirrus because the cloud retrieval algorithms may confuse thin cirrus with noise and remove them from the product output (Cazenave et al., 2019). Additionally, ground-based sensors, which are limited to a few land sites, struggle to see thin cirrus located high above convection or other cloud layers. Aircraft measurements are not representative of the global tropics due to limited sampling in space and time. Although there have been significant efforts to increase the quantity and quality of tropical observations (e.g., Yoneyama et al., 2013; Jensen et al., 2017; Houze & Betts, 1981, etc.), there is still a large gap in our understanding of the tropical cirrus life cycle, which impacts its representation in numerical simulations. Here, we analyze the simulated ice cloud populations, interpreting them in terms of an aggregate cirrus life cycle.

GSRMs have several properties that are advantageous to studying tropical cirrus. Un-

like conventional climate models with horizontal grid spacings of 25–200 km, GSRMs have sub-5 km grid spacing that enables them to explicitly simulate deep convection and its detrainment of ice into the upper troposphere, as well as better representing the mesoscale gravity wave spectrum and orographic features. These models also output variables with high spatiotemporal frequency, which provides a more detailed picture with higher realism than that from observations. Therefore, GSRMs have the potential to act as a surrogate for the real atmosphere and answer scientific questions about physical characteristics of tropical cloud populations and the aggregate life cycle of tropical cirrus. However, before we can use GSRMs to try to answer such questions, we must evaluate their performance compared to available observations. We focus on three regions of frequent convection: the TWP near Manus, Papua New Guinea and near Nauru Island (NAU) as well as the convectively-active Sahel (SHL) region in west Africa. The TWP is our main focus, but we include the other two regions for comparison to include different types of convection (land convection in the Sahel and less active ocean convection near Nauru Island). Each region has a significant amount of simulated deep convection and thin cirrus.

1.1 Archetypical life cycle of tropical cirrus

Convection plays a significant role in the formation and composition of tropical cirrus clouds (Fueglistaler et al., 2009). Houze (1981) describes the idealized life cycle of a typical tropical mesoscale convective system, which begins with a narrow core of deep convection in the formation stage that then matures and spreads into a system with stratiform precipitation and cirrus outflow. As the system weakens, the stratiform precipitation persists but tends not to reach the ground. Finally, the upper-level clouds break up and thin in the dissipating stage (Houze, 1981). During this evolution, the cloud system has notably different effects on the reflected shortwave and outgoing longwave radiation at the top of atmosphere (TOA) due to the changing amount of condensed water, particularly ice, in the vertical column and the change in the associated optical depth. We focus on the radiative impacts of the life cycle through the cloud populations present in each stage and their relative cloud radiative effect.

We use joint albedo-OLR histograms to characterize the cloud populations along with their TOA radiation balance in each model and the observations. Introduced by Hartmann and Short (1980), this histogram acts as a proxy for the cirrus life cycle. As the clouds progress from thick to thin (high FWP to low FWP), they follow a specific path in the albedo-OLR plane (Hartmann & Berry, 2017). An individual cirrus cloud layer may follow this life cycle path in the albedo-OLR plane (Gasparini et al., 2019). However, our proxy does not make the assumption of following individual cloud systems, but rather it is a statistical comparison between models and observations, revealing the behavior of clouds in each.

The overall radiative properties of tropical cloud fields integrate over all phases of the cirrus life cycle to be neutral in the TWP. The observed cancellation of LW and SW radiation has been well-documented but is still not well understood (e.g., Ramanathan et al., 1989; Hartmann et al., 2001; Kiehl, 1994). Ackerman et al. (1988) first showed that cirrus with an optical depth less than $\sim$5 have a net warming effect since they absorb more longwave (LW) radiation than they reflect shortwave (SW) solar radiation at TOA. Conversely, thick anvils and deep convective clouds reflect more SW radiation than they absorb LW radiation, resulting in a net cooling effect. In the TWP and NAU, the horizontal and temporal expanse of cirrus clouds with slightly positive cloud radiative effect (CRE) nearly cancel out the large negative CRE from relatively infrequent deep convective events. In this study, we analyze whether GCRMs capture this observed neutrality in the TWP and NAU regions.

1.2 TTL Cirrus

We also investigate the representation of cirrus in the tropical tropopause layer (TTL). The TTL is a transitional layer from troposphere to stratosphere, having properties of both (Highwood & Hoskins, 1998a). Here, the TTL is defined as the layer from 14 to 18 km above sea level. TTL cirrus are the highest clouds in the tropics. They are thought to play an active role in the thermodynamic structure of this layer and in setting lower-stratospheric water vapor concentrations.

The TTL is characterized by slow mean ascent from the ascending branch of the Brewer-

Dobson circulation, which drives the exchange of water vapor and other atmospheric tracers between the troposphere and stratosphere (Fueglistaler et al., 2009). For this reason, the TTL has been called the "gateway to the stratosphere" (Brewer, 1949). Convection penetrating the TTL and TTL cirrus may hydrate or dehydrate the TTL depending on the environmental saturation and cloud structure below the TTL (e.g., Dinh et al., 2014; Jensen & Pfister, 2004; Virts & Houze, 2015). Since water vapor is a potent greenhouse gas, changes in the stratospheric water vapor content have serious implications for future warming (Dessler et al., 2016).

Nugent et al. (2021) investigate the injection of ice into the upper troposphere, a possible source of ice for TTL cirrus formation, and the effect of convection on tropical cirrus. This study investigates the life cycle of tropical cirrus in GSRMs after formation. We compare the results to available observations, but thin cirrus or cirrus above convection are difficult to measure. TTL cirrus are difficult to characterize from in situ measurements and radar-lidar retrievals because of their high altitude and thin optical depths (Cazenave et al., 2019). TTL cirrus may have a stronger impact on the top of atmosphere energy balance than cirrus lower in the atmosphere. A better understanding of the radiative processes related to tropical cirrus is critical to improve our understanding of the Earth's energy balance and reduce uncertainty in future climate predictions (Sassen et al., 2009).

Although there have been significant efforts to increase the quantity and quality of tropical observations (e.g., Yoneyama et al., 2013; Jensen et al., 2017; Houze & Betts, 1981, etc.), there is still a large gap in our understanding of the TTL and tropical cirrus in today's atmosphere. Proper representation of the properties of tropical cirrus, especially cloud amount and hydrometeor distribution, is a key issue for improving climate models (Inoue et al., 2010). However, climate models typically have low horizontal resolution and simple ice microphysics parameterizations that lead to large differences between models. GSRMs do not use a convective parameterization but still parameterize sub-grid processes such as cloud microphysics. Ice microphysics is not well-represented in models due to the complexity of ice properties and the high computational overhead of complicated microphysical schemes.

This study evaluates the fidelity of GSRMs in their representation of tropical cirrus and ice cloud processes.

In Chapter 2, we begin with a description of the study domain, GSRMs, and the data used for comparison. We also include a description of a few key methods used in this study in Chapter 2.4–2.5. The aggregate life cycle of tropical cirrus in the TWP region for GSRMs compared to satellite observations are presented in Chapter 3. In Chapter 4, we include two more tropical regions for a regional comparison of the life cycle of tropical cirrus in GSRMs between land convection in the Sahel and oceanic convection in the TWP and Nauru. Chapter 6 summarizes our conclusions and discusses future work.

Chapter 2

METHODS AND DATA

2.1 Study Domains

We subset the global simulations and observational data into three 10° × 10° latitude-longitude regions in order to capture the characteristics of the tropics with minimal storage requirements. Despite their relatively small area, these three regions each contain substantial model output (at least 66,000 grid points) and offer a solid foundation for studying the simulation of tropical cirrus. Figure 2.1 shows the locations of these regions: (a) the Sahel (SHL) in west Africa; (b) the main TWP region near Manus Island, Papua New Guinea; and (c) a secondary region in the west Pacific near Nauru Island (NAU). Each region was chosen for its climatic significance and included an observational site offering a comprehensive set of ground-based observations for future work. We analyze how well the models capture differences in tropical cirrus statistics between these three regions (see regional comparison, Chapter 4).

The main region of interest for this paper is the TWP (Figure 2.1b). This oceanic region has the warmest sea surface temperatures in the world's oceans (Figure 2.1), which produces high near-surface humidity and moist static energy resulting in frequent deep convection. This region is a subset of the larger Tropical Western Pacific which generally includes 12–20°N/S of the equator from 130°E to 180°E (e.g., Gasparini et al., 2019; Hartmann & Berry, 2017). The 10° × 10° latitude-longitude TWP region experienced typical amounts of precipitation in 2016, with only a weak MJO in mid-August and slight La Niña conditions over the whole 40-day period. Since these are typical climatological conditions, we can more easily compare model output for the DYAMOND time period to the climatological observations.

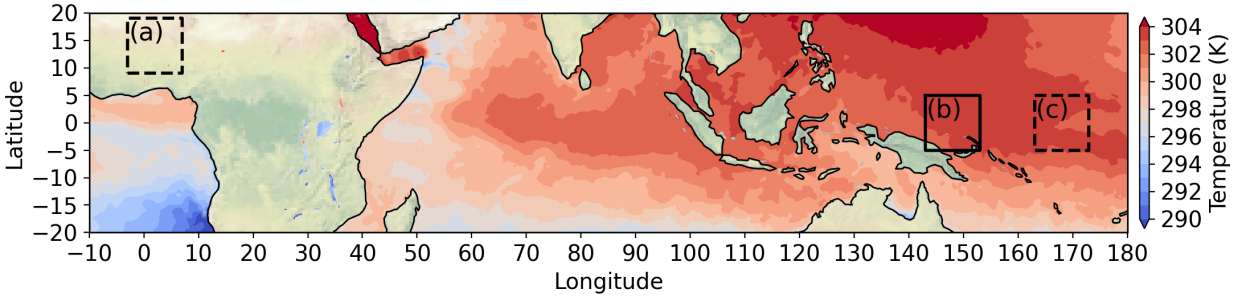

Figure 2.1: The three regions used in this analysis are (a) the Sahel (SHL; 3°W–7°E, 9°N–19°N), (b) Manus, Papua New Guinea (TWP; 143°E–153°E, 5°N–5°S), and (c) Nauru Island (NAU; 163°E–173°E, 5°N–5°S). The shading shows the initial sea surface temperatures in the DYAMOND models on 1 August 2016.

The NAU region (Figure 2.1c) lies directly east of the TWP. This region has less deep convection so, unlike in the TWP, the cirrus clouds are usually remotely generated (Long et al., 2016; Mace et al., 2006).

The third study domain, SHL, is located over Niamey, Niger in the Sahel region during the convectively-active West African Monsoon. This region was chosen to include the drier climate of the Sahara to the north of the $10° \times 10°$ region as well as the moister climate to the south (Figure 2.1a). The infrequent yet strong continental convection in the SHL is driven by solar heating and thus has a much different type and texture than in the oceanic regions (Liu & Zipser, 2005).

2.2 DYAMOND

This study uses outputs from GSRMs that participated in the DYnamics of the Atmosphere general circulation Modeled On Non-hydrostatic Domains (DYAMOND) project. The DYAMOND project was the first to compare the evolution of GSRMs over the same 40-day period (1 August 2016–10 September 2016) from the same initial atmospheric state defined by ECMWF reanalysis. From this initial state, the models were allowed to run freely with explicit deep convection using their own microphysics schemes, radiation, and dynamical

cores (Stevens et al., 2019), forced by the observed time-varying pattern of sea-surface temperature. DYAMOND provides an opportunity for an intercomparison of tropical cirrus and the life cycle of convective systems in several GSRMs over the same time period. Because the GSRMs are free running, we compare the model output statistically rather than comparing specific weather systems. We disregard the first two days of model output for all models as a spin-up period for cloud processes.

We focus on four models: Nonhydrostatic ICosahedral Atmospheric Model (NICAM), Finite Volume on a Cubed Sphere (FV3), ICOsahedral Nonhydrostatic model (ICON), and System for Atmospheric Modeling (SAM). Hereafter, these four models are collectively referred to as NFIS. We have the 3D output for NFIS and coarsened 2D output for the rest of the DYAMOND models (see Table 2.1).

Table 2.1: List of DYAMOND GSRMs used in this study by their acronym, horizontal grid spacing, and availability of ice/snow/graupel for 3D water content and 2D integrated water path.

	Grid	3D WC			2D WP		
Model	spacing	I	S	G	I	S	G
NICAM	3.5 km	X	X	X	X	X	X
FV3	3.25 km	X			X	X	X
ICON	2.5 km	X			X	X	X
SAM	4 km	X			X	X	X
ARPNH*	2.5 km				X		
IFS*	4 km				X	X	-
MPAS*	3.5 km				X	X	X
UM*	5 km				X		

* Coarsened model output 0.1° resolution used

- Graupel not included in microphysics scheme

For our study, we use 2D variables at 15 min intervals such as precipitation, available

integrated water paths (listed in Table 2.1), and SW and LW fluxes at TOA. For some 2D comparisons, we use output coarsened to a $0.1^\circ \times 0.1^\circ$ grid area from all of the DYAMOND models.

We also use the 3-hourly 3D output of temperature, hydrometeor mixing ratios (available frozen hydrometeors listed in Table 2.1), specific humidity, vertical velocity, pressure, and height. The vertical grid spacings, including those in the TTL, are similar between models. Of the models in this study, NICAM provides the finest vertical grid spacing in the TTL with 10 vertical levels within the 14–18 km TTL. FV3, ICON, and SAM all have 8 levels within the TTL.

Figure 2.2a shows a typical snapshot of ice water content (IWC) from FV3 in a $10^\circ \times 10^\circ$ latitude-longitude area for the TWP. Figure 2.2b zooms in on a subset to show the detail of one particular anvil cloud system from the subset of 3D columns outlined in red. The IWC is plotted with darker shading indicating more ice mass in a particular grid cell. This image demonstrates the detail and complexity of simulated cloud systems afforded by the high resolution. A convective core is surrounded by anvil outflow and thinner cirrus, with underlying low clouds.

As expected dealing with big data, we encountered a few minor file output errors in the DYAMOND GSRMs worthy of mentioning. SAM output of column-integrated water paths experienced a compression issue leading to a loss of significance at very small values. We use a smoothing function to adjust for this compression error without loss of meaning. Similarly, the distribution of FWP in ICON appears noisy for small values, which may also result from data management issues relating to file structures. These file issues are minor and only affect columns with either very small amounts of frozen condensate or no ice-phase clouds.

2.3 Data

We use data from two sun-synchronous satellites and one geosynchronous satellite to capture the properties of tropical clouds from past observations. The CALIPSO-CloudSat-CERES-MODIS (CCCM) merged product combines satellites in the A-train constellation, which

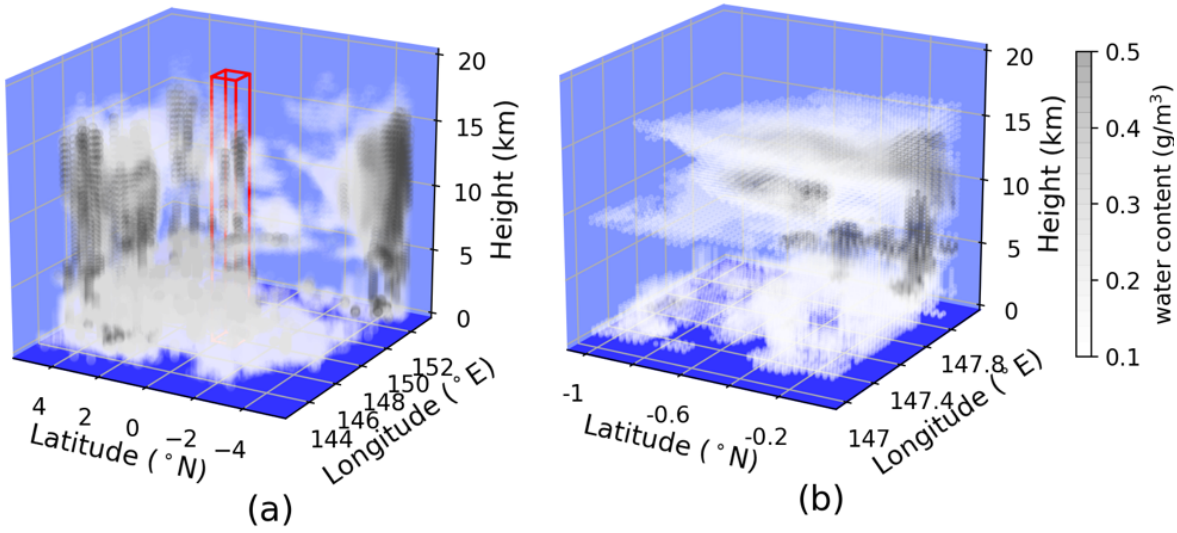

Figure 2.2: Snapshot of cloud water content (g/m^2) in FV3 at 07:00 on 24 August 2016 local time in the TWP region. The convection produced by explicitly resolved deep convection is shown for (a) the entire $10° \times 10°$ in the TWP and (b) a $1° \times 1°$ subset denoted by the subset of columns outlined in red in (a). Note, the latitude is flipped for better visualization. The value at each grid point is plotted separately to show the detail provided by the 3.25 km horizontal grid spacing.

passes over the equator at 01:30 and 13:30 local time (Stephens et al., 2002). The CCCM product provides collocated cloud microphysics and TOA radiative fluxes from July-August-September 2007–2010. We use this daytime values from this dataset (13:30 local time) when albedo can be measured. The CCCM data set has a horizontal footprint of roughly 30 km (Kato et al., 2011).

For higher-resolution measurements of IWC and IWP, we use synergistic combined lidar and radar retrievals from DARDAR (Delanoë & Hogan, 2008, 2010). The DARDAR product combines CloudSat, CALIPSO, and MODIS satellite measurements to derive microphysical properties of clouds. DARDAR combines the retrievals from both radar and lidar to get ice-cloud properties, which agree with in situ flight data (Deng et al., 2013). With its fine horizontal spacing of $\sim$ 1.1 km and a vertical resolution of 60 m (Sokol & Hartmann, 2018),

DARDAR is able to capture optically thin cirrus clouds with the lidar as well as the optically thicker cirrus near convective cores that can be seen by the radar. We use the both the daytime and nighttime values from the 2009 July-August-September data. For both oceanic regions (TWP and NAU), there was 50% more precipitation in August 2009 compared to August 2016 according to ECMWF reanalysis. Because of the natural variability between two years, the DYAMOND output in the oceanic regions may appear to underestimate convection compared to the DARDAR data. They have a higher uncertainty for thin or isolated cirrus because optically thin clouds are visible with only the lidar (Cazenave et al., 2019).

Since the A-train only pass over the tropics only twice daily, we use the daily radiative fluxes from the geosynchronous CERES Synoptic 1-degree (SYN1) product (Doelling et al., 2016a, 2016b). CERES SYN1 covers the 1 August - 10 September period from $2000 - 2019$. CERES SYN1 data has a $1^\circ \times 1^\circ$ horizontal resolution with an approximate uncertainty of 3 W/m^2 (Kato et al., 2018).

For comparisons between DYAMOND output and observations described here, we coarsen the model output to $0.3^\circ \times 0.3^\circ$ to match CCCM or $1^\circ \times 1^\circ$ to match CERES. Since the footprint of the DARDAR retrieval is similar to the model grid spacings, the model output is not coarsened for comparisons with DARDAR.

2.4 FWP Categorization

The life cycle of tropical convective systems for each model is qualitatively and quantitatively discussed in this paper. To quantify the life cycle, we classify each column according to its column-integrated frozen water path (FWP), where FWP is the sum of ice, snow, and graupel water paths. We define three life stages that approximately correspond to (1) Deep Convection, (2) Anvil/Thick Cirrus, and (3) Thin Cirrus. The categories (abbrev. CAT) are as follows:

The thresholds chosen here are based on an order of magnitude argument derived from general behaviors of columns with the specified FWP and examples in the literature (e.g.

FWP Categories:

CAT 1	Deep convection		FWP	≥ 1000 g/m^2
CAT 2	Anvils	$10 \leq$	FWP	< 1000 g/m^2
CAT 3	Thin cirrus	$0.1 \leq$	FWP	< 10 g/m^2
	Cirrus-free		FWP	< 0.1 g/m^2

Sokol & Hartmann, 2018). Columns characterized by deep convection have an FWP of 1000 g/m^2 or more and contain the convection that penetrates the TTL. Nugent et al. (2021) show that the frozen water mass transport into the TTL is dominated by deep convective events. Thus, columns with FWP ≤ 1000 g/m^2 contribute only a small fraction of frozen mass into the TTL.

The GSRM radiative transfer schemes operate on individual columns for computational efficiency. Consequently, our analysis largely focuses on column-by-column statistics, not horizontal relationships between columns. Each column falls into a FWP category and has an associated SW and LW CRE. Although we do not have output of optical depth for most models, the albedo can be used as a proxy for optical depth; for example, clouds with higher albedo are generally optically thicker. The cloud top height is revealed through the OLR values; thus, we can gain insight into cloud types through these two 2D variables. A schematic for cloud populations in relation to albedo and OLR is shown in Figure 2.3. The typical life cycle roughly aligns with the black arrow in Figure 2.3, starting with deep convection progressing through anvils to thin cirrus. The life cycle path in the albedo-OLR plane does not show the specific life cycle of a particular convective system but instead represents a probabilistic or aggregate life cycle. The joint albedo-OLR histogram is a useful qualitative and quantitative approach to the effect of clouds and their life cycle on the radiation budget. Using albedo restricts our analysis to only daytime values, specifically 10 am–2 pm local time in the models, which eliminates any anomalies occurring near dawn and dusk. The joint albedo-OLR histograms have a maximum probability distribution at

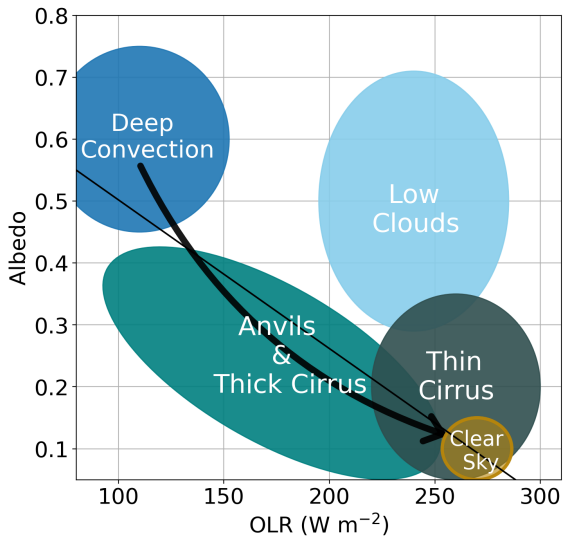

Figure 2.3: Schematic of cloud types in the albedo-OLR plane. The four main categories are (1) Deep Convection, (2) Anvil/Thick Cirrus, (3) Thin Cirrus, and (4) Low Clouds. Clear sky (orange circle) overlaps with the Thin Cirrus category. The black arrow shows the idealized aggregate life cycle as the convective clouds thin over time.

the clear-sky values (orange circle in Figure 2.3).

For comparisons to observational data and previous studies, we use the model output of hydrometeor mixing ratios to calculate frozen water content (FWC) and liquid water content (LWC). For FV3, ICON, and SAM, only cloud ice and cloud water were saved for the 3D hydrometeors, so we cannot calculate the FWC. Only NICAM provided 3D fields of snow and graupel, allowing us to compute FWC. So we show vertical profiles of cloud ice, snow, and graupel in NICAM to demonstrate how TTL FWC differs between cloud types (Figure 2.4). Above 14 km, snow and graupel in NICAM only make up a significant portion of the total frozen water in the rare areas with vigorous deep convection (Figure 2.4a). In columns with anvils or thin cirrus in NICAM, neither snow nor graupel affect the total amount of condensate in the TTL (Figure 2.4b–c). We assume the IWC is a decent representation of FWC in the TTL for anvils and cirrus in models that do not output 3D snow or graupel.

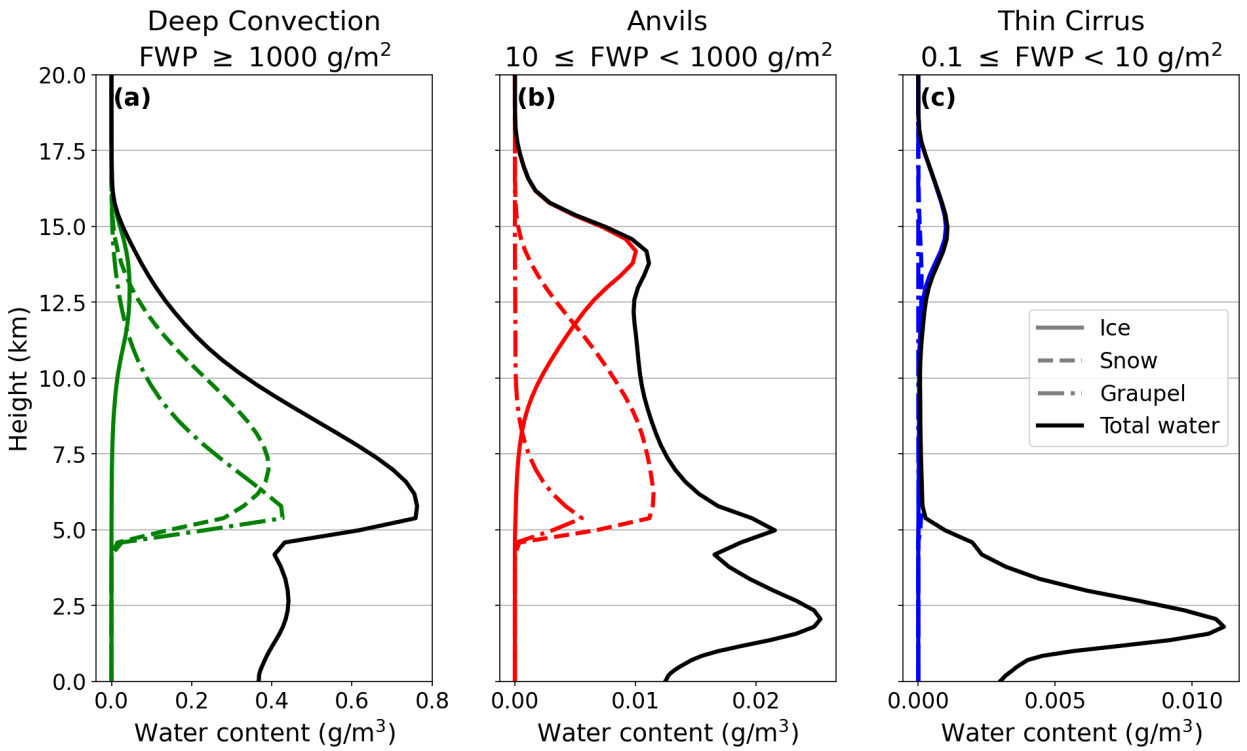

Figure 2.4: Vertical profiles of water content (g/m^3) for NICAM showing the breakdown between ice (solid), snow (dashed), and graupel (dot-dashed) in areas of (a) Deep Convection (green), (b) Anvil/Thick Cirrus (red), and (c) Thin Cirrus (blue). The total water content, including liquid, is shown in the solid black line. The x-axis is different for each plot.

Thus, we assume that the TTL IWC for FV3, ICON, and SAM decently represents the TTL FWC for anvil and cirrus clouds. However, TTL IWC in areas of deep convection may underestimate the total FWC because snow and graupel make up a majority of total mass of frozen condensate for NICAM (in aggrement with Nugent et al., 2021). So, IWC in the TTL for FV3, ICON, and SAM cannot accurately represent FWC for deep convection.

2.4.1 Determining Clear Sky

The DYAMOND models produce few columns that are truly ice-free. The model microphysics schemes typically retain small amounts of FWC, so some models produce physically

inconsistent amounts of cloud cover. Therefore, we impose a lower threshold for water content and FWP, below which we consider the column to be free of ice-phase clouds. Specifically, we define clear-sky points as those with FWC less than 5×10^{-4} g/m^3 since few FWC measurements from aircraft or satellite data are observed below this level (Deng et al., 2013). Assuming a minimum vertical grid spacing of about 200 meters, the column-integrated water path must be on the order of 0.1 g/m^2 for the volume to be cloudy. DARDAR does not detect FWP values less than 0.1 g/m^2. The frequency of thin cirrus clouds is sensitive to this threshold in all of the models.

2.5 Cloud Radiative Effects

For most of this analysis, we ignore underlying low liquid clouds since they have little effect on TOA OLR; however, they can have a significant impact on albedo. We investigate the CRE for each model and cloud population using the FWP categories. The SW CRE is defined as the difference between albedo in a given column and the clear-sky albedo multiplied by the average solar insolation, which differs based on latitude. This constant is 413.2 W/m^2 in the TWP and NAU regions and 435.3 W/m^2 in the SHL region.

The albedo, SW CRE, and LW CRE are computed as follows:

$$\text{albedo} = \frac{\text{SW}_{\text{reflected}}}{\text{SW}_{\text{incoming}}} \tag{2.1}$$

$$\text{SW} = \text{S}_{\text{const}}(\text{albedo}_{\text{clear-sky}} - \text{albedo}) \tag{2.2}$$

$$\text{LW} = (\text{OLR}_{\text{clear-sky}} - \text{OLR}) \tag{2.3}$$

We calculate the clear-sky values of OLR and albedo from columns near noon with a combined FWP and LWP below 0.1 g/m^2. Within these clear-sky columns, the TOA LW and SW radiation may vary considerably due to the amount and distribution of water vapor in a column. The presence of ice in the TTL below the clear-sky threshold should have negligible effects on the TOA energy budget at such small concentrations (see Chapter 2.4.1). The CRE calculations have an error of approximately ± 15 W/m^2, most of this uncertainty arises

from the calculation of clear-sky fluxes because not all models output the clear-sky LW and SW radiative fluxes.

Berry and Mace (2014), among others, demonstrate that an abundance of thin ice clouds produce a warming effect at TOA while thicker convective clouds produce a negative CRE. They also find that the mean net CRE is a function of cirrus FWP and can have a warming effect as large as 40 W/m^2 (corresponding to a FWP of $20 - 60$ g/m^2) which then decreases as the cloud thickens, reaching 0 W/m^2 at around 200 g/m^2. Thus, the categories used in this study associate CAT 1 with a strong cooling effect and CAT 3 with a warming effect while CAT 2 has a mixture of clouds with both effects.

Chapter 3

THE AGGREGATE LIFE CYCLE OF TROPICAL CIRRUS IN THE TWP

3.1 Cloud Populations

The distribution of albedo and OLR show cloud populations in the models and observations, along with the model biases. Figure 3.1 shows the joint albedo-OLR histogram for observational data and model output, showing the main cloud populations in the TWP as defined in the schematic (Figure 3.1f).

The CCCM histogram (Figure 3.1a) shows a concentration of values in the lower right, where low albedo and high OLR indicate clear-sky columns. There are fewer values as albedo increases and OLR decreases following a banana-shaped curve up to deep convection. In the deep convection region, there is a local peak in the distribution by low OLR and high albedo values. The deep convective columns contain an albedo-OLR pairing composed of deep convection with associated thick anvils inside the 30 km CCCM footprint. The models are coarsened to match the 30 km footprint in Figure 3.1. In comparing the albedo-OLR histograms for each model, we look for the three properties that are key characteristics of the observations: (1) a clear sky peak, (2) a secondary peak in deep convection, and (3) a banana-shaped distribution.

First, all of the models successfully capture the clear-sky peak at the high OLR-low albedo area though FV3, ICON, and IFS have slightly higher clear-sky OLR values. Second, FV3, MPAS, and UM capture the local maximum in the deep convective region. Third, NICAM and IFS match the general shape of the histogram very well even though they do not capture the secondary peak in deep convection. Finally, ICON, SAM, and ARPNH all fail to simulate the secondary peak in deep convection and do not match the banana-shaped

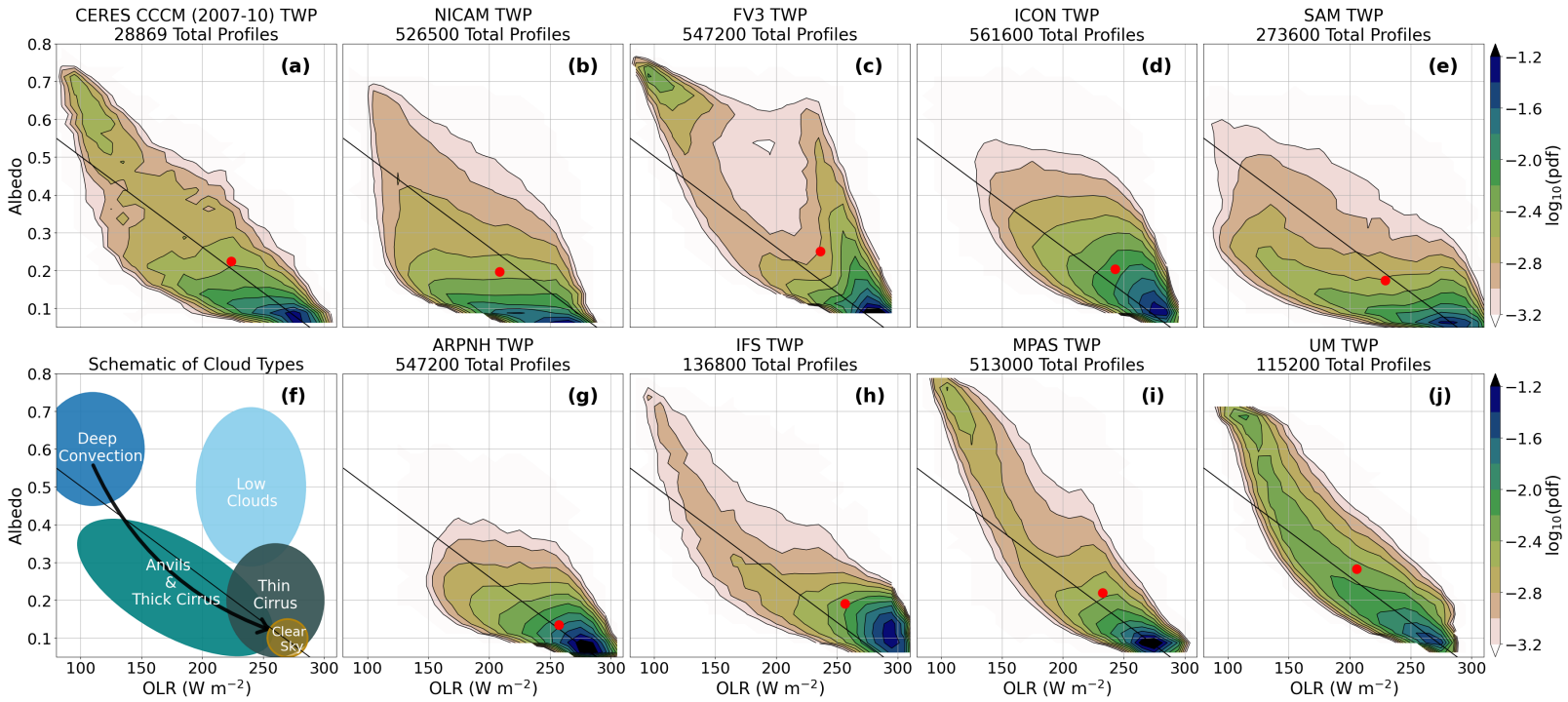

Figure 3.1: Density plot of albedo and OLR for (a) CCCM and (b–e,g–j) the DYAMOND models for days 3–40. The schematic of cloud types is reproduced in (f). Model output averaged over 0.3° to match the CCCM footprint. There are 32 and 27 evenly spaced bins for the OLR and albedo, respectively The red dot indicates the mean albedo-OLR pairing for the distribution. Neutral CRE is calculated from observation as the black line.

distribution of the observations.

It may be that ICON and ARPNH do not appear to have deep convection because their deep convective cores are not surrounded by sufficient thick, cold anvil in the 30 km $\times$ 30 km area. However, it is likely that these models do not generate sufficient FWP and anvil outflow from deep convection or convection does not reach cold enough cloud-top temperatures. SAM also fails to produce clouds consituting deep convection in the albedo-OLR plane. SAM has convection reaching the upper troposphere shown by the low OLR values, but the convection is not optically thick. This is likely due to insufficient FWP values so that the albedo is too low for deep convection. Therefore, SAM tends to favor the formation of weak convection or anvils rather than deep convective towers. In contrast, FV3 generates a population of clouds with relatively high albedo and high OLR values. This is likely due to a concentration of low and mid-level clouds, which are unique to FV3.

MPAS and UM capture all of the key characteristics observed in the TWP. NICAM, FV3, and IFS also capture a couple key traits of cloud populations in the TWP, but ICON, SAM, and ARPNH deviate greatly from the observed cloud populations.

Another key trait of clouds in the TWP is the near zero CRE noted in Hartmann et al. (2001) as a balance between the SW cooling effect of convective towers and the small LW warming effect of cirrus. In the CCCM data, this net neutrality is evident by the intersection of the black line of neutral CRE and the red dot, which marks the mean albedo and OLR (Figure 3.1a). The black line from the observations is replicated on all plots as a reference point. A mean value above (below) the black line signifies an overall cooling (warming) effect. Most models have a mean OLR and albedo reasonably close to zero. Here, the models approximate the observed neutral TOA balance of LW and SW fluxes within 11%. Therefore, despite major differences in the cloud populations and shapes of distributions, the models are simulating the overall balance of OLR and reflected SW at TOA well.

The models simulate clouds differently from each other and observations but are able to capture some key characteristics of the observations. Despite the different cloud populations, the overall CRE is close to observations. This leads us to ask how do these differences arise?

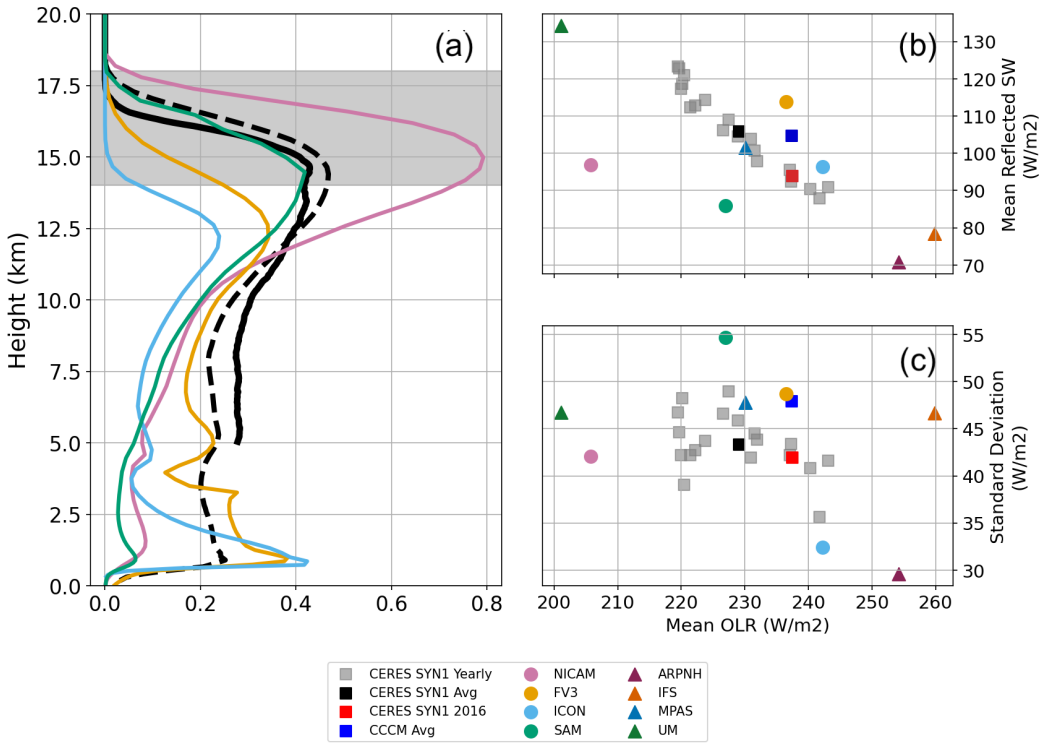

Figure 3.2: (a) Vertical occurrence of clouds for each model from days 3–40 compared to observations from DARDAR and CCCM. For the models, only cloud ice is used to calculate cloud fraction; the observations implicitly include all frozen hydrometeors. (b) Daily mean versus standard deviation of OLR from days 3–40. (c) Daily mean OLR plotted against daily mean reflected SW radiation. Model output is coarsened to hourly and $1^\circ \times 1^\circ$ area to match CERES SYN1 data over the region.

3.2 TOA Radiation Balance

From the albedo-OLR histograms, each model tends to generate a unique cloud distribution. Some models capture the convection well while others favor anvils and cirrus. These differences are reflected in both the vertical structure of clouds and the radiative fluxes over the 40-day period. We begin with a discussion of observed characteristics of cloud profiles and then compare the model output to observations.

Observations of tropical cloud fraction tend to have three peaks: near the top of the

boundary layer, at or just above the freezing level, and in the upper troposphere (Hollars et al., 2004). Virts, Wallace, Fu, and Ackerman (2010) show that the cloud occurrence for upper troposphere cirrus maximizes in the $14 - 15$ km layer, which corresponds to the base of the TTL. Model profiles in Figure 3.2a are consistent with this conclusion for NICAM and SAM, but FV3 and ICON peak well below the TTL at $\sim$12.5 km. Note, the vertical cloud occurrence was calculated using the cloud threshold of 5×10^{-4} g/m^3 (See Chapter 2.4.1). Although FV3, ICON, and SAM do not save 3D output of snow or graupel, the cloud fraction from cloud ice alone should be sufficient to roughly describe the total frozen cloud fraction. Even though the frozen mass is dominated by snow and graupel, snow and graupel are often collocated with cloud ice, so we expect the cloud fractions to be similar.

The vertical cloud occurrence in Figure 3.2a show that NICAM has too many clouds in the upper troposphere and TTL but too few low clouds. FV3 has too few upper-level clouds and too many low clouds, but it gets the mid-level cloud occurrence right. ICON has a smaller cloud fraction for ice and mixed phase clouds. ICON also has very little ice clouds extending into the TTL. This is consistent with the albedo-OLR joint histogram (Figure 3.2). SAM is reasonably close in frequency and shape to the observed cloud occurrence.

These vertical profiles of cloud occurrence determine TOA radiative fluxes. We juxtapose this relationship in Figure 3.2 with the vertical structure in 3.2a and key properties of the radiative fluxes in 3.2b and c. We include CCCM, DARDAR, and CERES SYN1 satellite observations here to show the range of possible observed values of cloud occurrence as well as LW and SW fluxes at TOA. Twenty years of CERES SYN1 data (gray squares) show the interannual variability. The model spread should ideally be contained within the range of natural annual variability, but many of the models lie outside of this range (Figure 3.2b–c). The models were coarsened to match the hourly and $1^\circ \times 1^\circ$ horizontal resolution of the CERES SYN1 data.

In Figure 3.2b, the relationship between mean OLR and reflected SW radiation seems to be linear across 45 W/m^2 in mean OLR and 35 W/m^2 in mean reflected SW radiation. MPAS, FV3, and ICON are relatively close to the scatter of observations. NICAM and SAM

fall well below the linear behavior of the observations. NICAM has a much lower mean OLR due to the prevalence of TTL cirrus. For SAM the amount of reflected SW radiation is too low because convection in SAM is optically thinner than the other models. UM, ARPNH, and IFS capture the linear quality if the observations were fit to a line but fall well outside the range of observed mean values. UM also has a low OLR because it had a larger population of deep convective and anvil clouds than any other model (Figure 3.1j). ICON and ARPNH have weak and infrequent convection causing the high mean OLR.

Figure 3.2c shows the standard deviation of OLR against the mean OLR. The standard deviation of OLR provides insight into the texture of convection since a larger standard deviation signifies bursts of deep convection and more variation in the amount of high cloud. Together, the mean and standard deviation of OLR describe the character of convection and cloud populations in each model. The observations cluster between 35–50 W/m^2 standard deviation in OLR but ICON, ARPNH, and SAM fall outside this range. ICON has weak convection, rarely penetrating the TTL and has corresponding high mean OLR and small standard deviation (consistent with Nugent et al., 2021). However, the clouds in ICON are fairly reflective (likely due to the high reflectivity of liquid clouds). SAM has too much variance, indicative of frequent, and perhaps short-lived, clouds that penetrate the TTL but are optically thinner than observed deep convection.

In both Figure 3.2, MPAS and FV3 appear to have no major biases in TOA OLR or reflected SW radiation in the 38-day model climatology. The models with significant radiative biases are NICAM (low mean OLR), SAM (too much variance in OLR), ICON (low variance in OLR), ARPNH and IFS (high mean OLR, low mean reflected SW, and low variance for ARPNH), and UM (low OLR with high reflected SW).

3.3 Categorization of Life Cycle

The life cycle of tropical cirrus is a continuous process, but we simplify the life cycle into three main stages or categories that roughly align with those from the schematic in Figure 2.3, excluding the low cloud population that does not contain frozen water. By breaking down the FWP into categories, we build a composite life cycle based on these statistical snapshots of each life stage.

The categories are plotted as different colors in Figure 3.3a–e corresponding to deep convection (CAT 1; green), anvils (CAT 2; red), thin cirrus (CAT 3; blue), and cirrus-free (gray). We differentiate thin cirrus from cirrus-free columns using the threshold FWP= 0.1 g/m^2 as described in Chapter 2.4.1. In this case, we also ignore LWP since our focus is on cirrus clouds.

The deep convective cores (CAT 1) occupy less than 11% of all columns in space and time in the observations but less than about 5% in the models (see the percentage of CAT 1 listed in Figure 3.3a–e). We use DARDAR due to fine horizontal resolution that is similar to that of the models, so the model output is not coarsened as it was with CCCM in Figure 3.1 and 3.2. The DARDAR measurements were taken during an August with with nearly 50% more convection than August 2016. Assuming all the extra precipitation comes from deep convection, a low estimate for the observations is approximately 7% occurrence of CAT 1. Even then, the models are underestimating

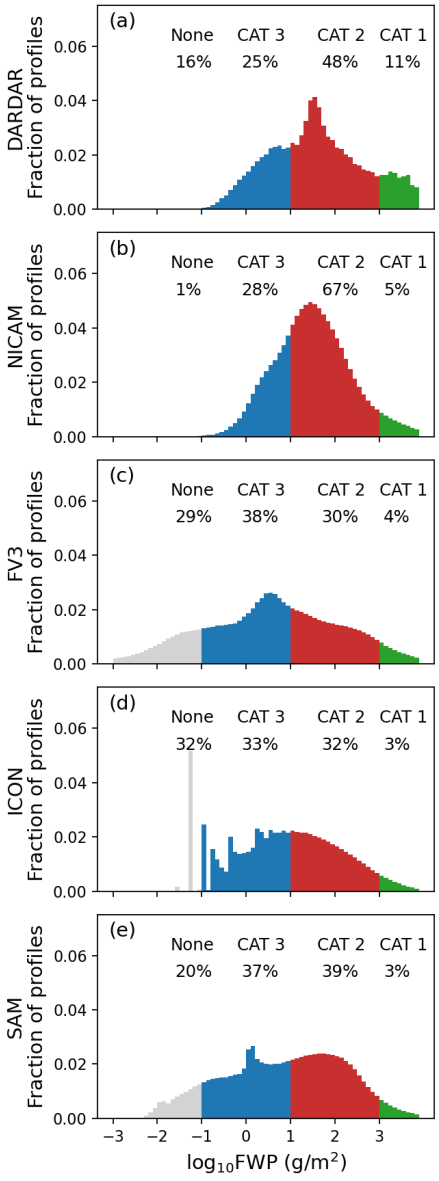

Figure 3.3: Total column FWP for (a) DARDAR and (b–e) model output from days 3–40 colored by the FWP categories: (green) deep convection, (red) anvil or thick cirrus, and (blue) thin cirrus.

CAT 1 by up to half as noted in Figure 3.3b–e.

CAT 2 (red in Figure 3.3) has the widest range of cloud types, including stratiform cloud decks, anvils, and optically thick cirrus. This category also occupies the most area in space and time, containing 37%–66% of all columns for the models and data. CAT 2 has the most variance in frequency of occurrence. We expect this because it contains the widest variety of cloud types.

CAT 3 (blue in Figure 3.3) includes TTL cirrus as well as thin cirrus at lower levels. CAT 3 occurs only slightly less often than CAT 2, ranging from 28% in the observations to 36% in SAM. CAT 3 frequencies have a better agreement between models and observations than CAT 2 frequencies.

There is a large range of histogram shapes in FWP among the models. The shape of the model histograms reveal the different ice properties of the models. NICAM most closely matches the shape of DARDAR and captures the peak FWP near 30 g/m^2. FV3 and ICON peak at a smaller FWP while SAM peaks at a larger FWP.

SAM has much more variance in OLR (Figure 3.2b)than the other models yet only 4% of columns have deep convection (Figure 3.3e). This variance must arise from weak convection and formation of anvils in the upper troposphere that falls into CAT 2 as shown by the peak in the FWP histogram near 100 g/m^2 (Figure 3.3a). This is also consistent with results from the joint histogram in Figure 3.1e in which SAM shows a tendency to generate anvil with cold cloud tops rather than deep convection.

ICON lacks of deep convection as seen in the vertical cloud occurrence (Figure 3.2a), especially convection penetrating the TTL. ICON's convective towers do not produce sufficient FWP, which in turn affects the CRE and the cloud distribution in the albedo-OLR plane (Figure 3.1d).

From the FWP CAT frequencies, we conclude that the models consistently have too few CAT 1 columns and slightly too many CAT 3. In general, the models do not generate sufficient frozen condensate mass associated with convection. Aside from NICAM, the models produce too little CAT 2. The ice cloud cover amount is sensitive to our choice of clear-sky

threshold. The spatial dominance of the maturing and dissipating stages of the ideal life cycle from Houze (1981) are consistent with our results.

3.4 Life Cycle Proxy

Breaking down the FWPs into categories allows us to construct an aggregate life cycle for each model and the observations. The median value of OLR and albedo for each category is plotted in Figure 3.4 with CAT 1 deep convection in the upper left corner progressing to CAT 2 anvils and ending with CAT 3 thin cirrus in the lower right. Each model follows a unique path from one category to the next in the albedo-OLR plane. The median values are used because (Berry & Mace, 2014) found that the mean value of IWP is a poor diagnostic of radiative properties of tropical cirrus. The models are kept at their native grid resolution to take advantage of the fine horizontal resolution provided by GSRMs, so the observations have a footprint about 6X larger than the models, but the CCCM FWP is calculated for the cloudy fraction of the footprint. The difference in resolution has allows the models to more precisely label columns into their categories (less mixing of cloud types in one 30 km $\times$ 30 km area).

The largest differences between models occur in CAT 2 with OLR ranging from 166–202 W/m^2 and albedo from 0.15–0.44. One major factor in albedo is the presence of liquid clouds because they are more reflective than ice clouds. SAM has substantial liquid clouds in CAT 2. NICAM has liquid clouds only associated with ice clouds and convection, but FV3 tends to have some liquid clouds underlying CAT 2 and 3 anvil and cirrus. ICON tends to have more liquid clouds underlying CAT 3 cirrus clouds. In CAT 2, SAM has the coldest cloud-top temperature (associated with the low OLR), followed by FV3, NICAM, then ICON. SAM tends to generate CAT 2 clouds with a peak in the FWP distribution at 100 g/m^2 whereas the other models peak at lower FWP values.

Berry and Mace (2014) find that the CRE transitions from cooling to warming around a FWP of 200 g/m^2. As FWP decreases further, the warming effect becomes stronger. The locations of the median values for each model are all above the black line of neutral CRE in

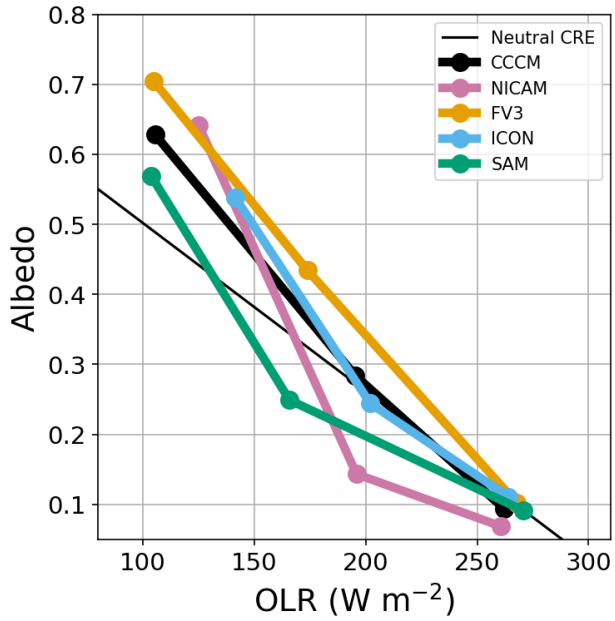

Figure 3.4: The median albedo-OLR pairing for each category is plotted as closed circles for the data and models. Models are not coarsened to match the CCCM footprint. CAT 1 is the upper-leftmost point and is connected to CAT 2 and then CAT 3 by straight lines, signifying the aggregate life cycle of tropical cirrus.

CAT 1. CAT 2 is where the transition from cooling to warming occurs and subsequently the models ranges from cooling in FV3 to warming in NICAM.

Figure 3.4 shows that FV3 and SAM have the lowest values of OLR for CAT 1, meaning that they produce tall convective towers with the coldest cloud tops. Despite its low OLR, SAM has a lower albedo than FV3, NICAM, or the observations, indicating that its convection is not as reflective or optically thick. ICON has the weakest deep convection, meaning it does not have convective towers that reach as high or are as reflective as the other models. This is consistent with the vertical cloud occurrences in Figure 3.2 and cloud populations in Figure 3.1. Despite differing occurrences of deep convection in each model, CAT 1 is important for bringing ice into the TTL, so this lack of deep convection may affect the subsequent frequency and properties of cirrus.

Chapter 4

REGIONAL COMPARISON

Here, we compare results from two other tropical regions with the TWP results to see how the models perform in these different yet climatically significant regions. For more details on the SHL and NAU regions, see Chapter 2.1.

4.1 Cloud Populations

The SHL has a much brighter surface than the dark ocean. The northern half of the SHL region is the high-albedo Sahara while the southern half has more vegetation and a lower surface albedo causing a larger variation in clear-sky albedo and OLR values and overall higher albedo than the ocean (see Figure 4.1a–e). In the SHL, most clouds lie below the line of neutral CRE in Figure 4.1a, denoting a stronger warming effect of clouds over the SHL. CCCM data also has fewer thick-anvil columns than the TWP as denoted by the gap in the histogram near 0.6–0.65 albedo and low OLR values. This cloud distribution is characteristic of the more sporadic deep convection in a drier environment.

Compared to the TWP, NAU has fewer deep convective columns and no secondary peak at low OLR-high albedo values. The mean CRE (red dot in Figure 4.1a) in NAU is above the line of neutral CRE, signifying a net cooling effect of clouds in NAU. This is likely due to the larger population of low clouds which are more reflective than extended cirrus clouds.

Even though the models do not match the observed cloud distribution shape, they do have the subtle regional shifts in cloud types. Over the 40-day period, the models settle into their own model climatology. The model climatologies identified in the TWP are consistent across the regions for all models. NICAM has frequent thin cirrus. FV3 has a large liquid cloud population. ICON and SAM do not have sufficient deep convection. There are two

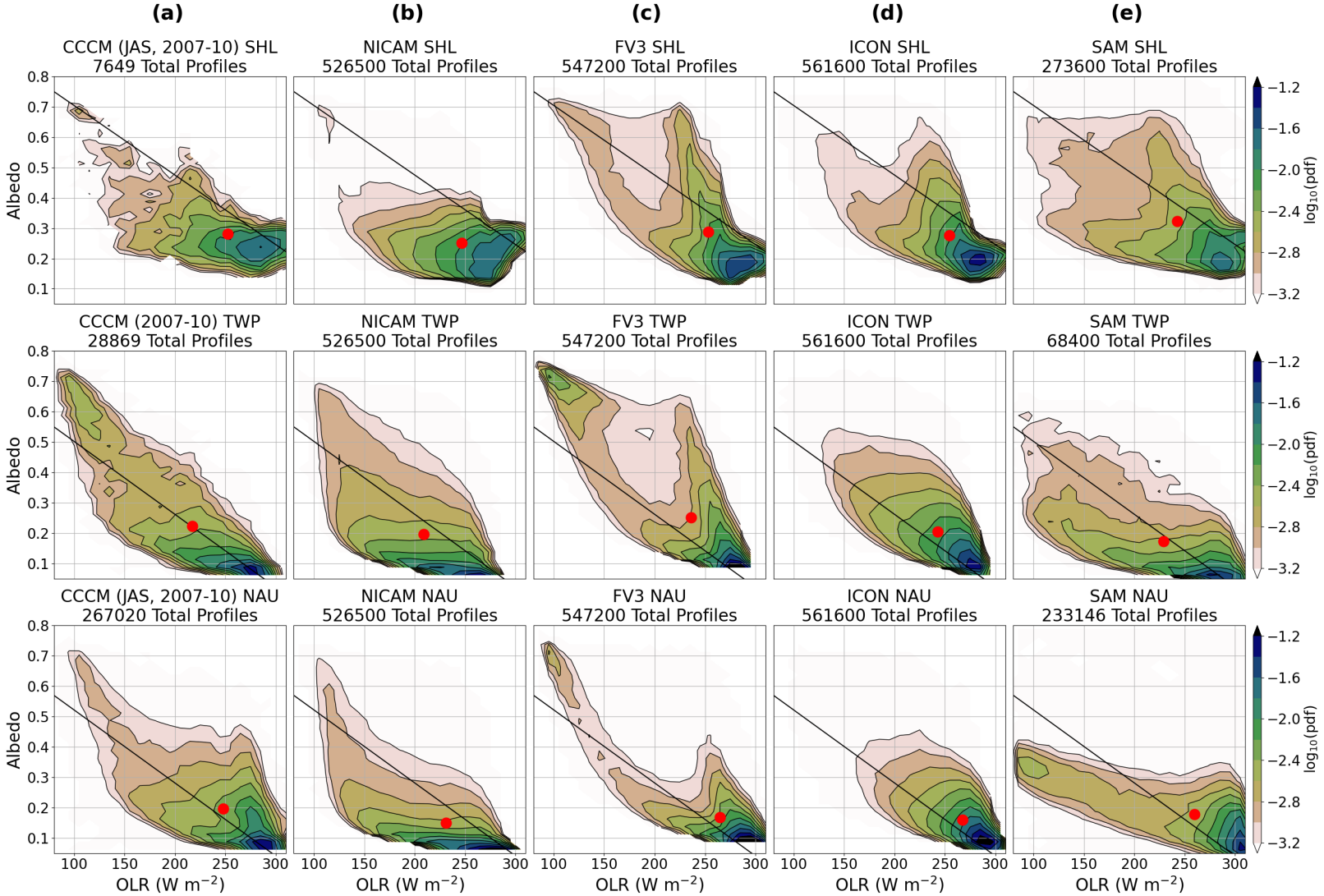

Figure 4.1: Joint albedo-OLR histogram for SHL (top), TWP (center), and NAU (bottom) for (a) the observations from CCCM and the model output from (b) NICAM, (c) FV3, (d) ICON, and (e) SAM. The black line of neutral CRE was calculated for each region from the observations.

key regional differences from the TWP for both the SHL and NAU. For the SHL, the major differences are (1) the higher and more variable clear-sky albedo and (2) fewer thick-anvil columns connecting deep convection to anvils and cirrus. In NAU, the major differences are (1) an increased low cloud population and (2) a weaker deep convective peak in the probability distribution. In the observations, there is a warming effect of clouds in the SHL and slight cooling in NAU. The models capture some but not all of these features.

NICAM captures both regional differences between the SHL and TWP and one in NAU. Figure 4.1b shows the distribution of albedo and OLR values for NICAM in the SHL (upper), TWP (center), and NAU (lower). NICAM has both of the regional characteristics of the SHL noted in observations. There is a gap between deep convection and thick cirrus in NICAM in the 0.45–0.6 albedo range, which is slightly lower than the observed gap in the SHL but qualitatively similar. In NAU, NICAM has the appropriate deep convection occurrence but has too few low clouds compared to the observations.

The distribution of albedo and OLR in FV3 is shown in Figure 4.1c. FV3 captures one of the regional differences between the SHL and the TWP: the higher variability in the clear-sky albedo-OLR values. FV3 does not separate deep convection from the anvil and cirrus cloud populations like we see the observations. As in the TWP, FV3 simulates a large population of low clouds with high albedo and high OLR values in the SHL. These low clouds are not observed in the SHL or TWP. In NAU, however, FV3 has fewer low clouds and secondary peak in deep convection not observed. Therefore, FV3 captures one characteristic of each region well.

The albedo-OLR histogram for ICON (Figure 4.1d) looks remarkably similar between regions. ICON has slightly more variation in clear-sky albedo-OLR values in the SHL than in the TWP, but not as much as observed. Since ICON does not have deep convection at low OLR and high albedo values, it cannot capture the observed separation of deep convective and cirrus cloud populations. There is no change in low cloud population from the TWP to NAU in ICON. In NAU, ICON has even fewer low OLR and high albedo values than in the TWP. This is consistent with vertical cloud occurrence in ICON from Figure 4.2 where

clouds were infrequent in the upper troposphere and rarely reached the TTL. Such clouds would not reach low OLR or high albedo values, varying little from clear-sky values as shown in Figure 3.2a and b for the TWP. Technically, ICON captures one regional difference in the SHL and NAU from the TWP; however, the shape of the histogram is unique and clearly much different from the observed distribution of cloud types.

Figure 4.1e shows that SAM has a wide range of cloud populations present between the regions. Comparing the SHL to the TWP, there is a larger variation in the SHL clear-sky albedo-OLR values but SAM does not capture the observed gap between deep convection and anvils. In the SHL, SAM simulates a variety of cloud albedo-OLR values from a high-albedo population of low clouds to a low OLR-low albedo population of thick anvils. In NAU, instead of missing a population of thick anvils like the observations, SAM generates only thick anvils and few instances of deep convection. Like observed, SAM also has more frequent low clouds in NAU, so SAM captures one characteristic difference for each region compared to the TWP.

The general behavior of each model dominates while the regional shifts are more subtle. For example, ICON and FV3 generate distinctive distributions that have clear similarities between regions. Nonetheless, the models do have subtle regional differences similar to those observed. Despite the excessive population of TTL cirrus, NICAM captures the major characteristics of the observed distribution of clouds. FV3 simulates deep convection well but has too many low clouds in the SHL and TWP where they are not observed. ICON has too little deep convection and SAM has difficulty generating values of high albedo. These model differences have an effect on the impact of clouds in the model overall. The mean CRE of each region is reproduced by most models in most regions. Like the observations, each model has a warming effect in the SHL while all but NICAM have a cooling effect in NAU. The mean CRE varies more in the TWP which has an observed neutral CRE, but each model falls within the uncertainty of a neutral estimated mean CRE.

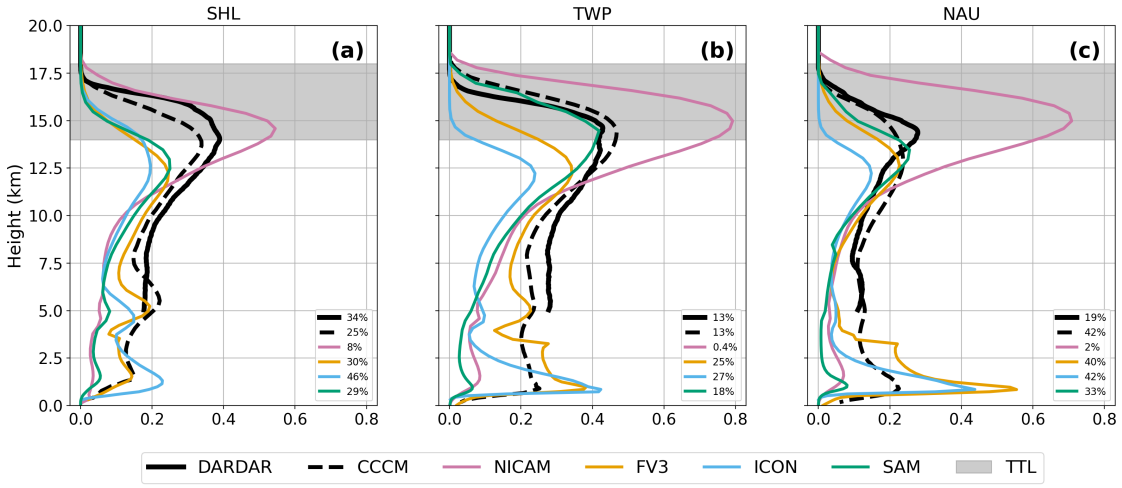

Figure 4.2: Same as Figure 3.2a but for the (a) SHL, (b) TWP, and (c) NAU. The clear-sky percentages are noted in the legend for SHL, TWP, and NAU respectively. The radar-lidar product from CCCM shows the combined liquid and ice-phase cloud occurrence.

4.2 Vertical Structure of Clouds

In the observations, all regions have a primary peak in cloud occurrence near the base of the TTL. The TWP has the highest cloud occurrence at all heights (Figure 4.2b) and the most cloud cover (time-area percent of cloudy columns) at nearly 87% as implied from the Figure 4.2 legend. The SHL (Figure 4.2a) has comparable vertical cloud occurrence in the TTL but much less surface cloud cover (66% in DARDAR and 75% in CCCM). There is also a stronger trimodal peak in the cloud occurrence in the SHL, characteristic of the region (Johnson et al., 1999). There are fewer TTL and mid-troposphere clouds in NAU but a stronger peak in cloud occurrence at the freezing level than in the other regions (Figure 4.2c).

FV3, ICON, and SAM reproduce the trimodal distribution of clouds in the SHL, but fail to simulate enough TTL clouds. In all regions, NICAM overestimates the cloud occurrence in the TTL and underestimates clouds in the lower troposphere. Compared to the TWP, each

model simulates fewer TTL and mid-troposphere clouds in NAU consistent with observations.

The models each have a consistent characteristic vertical structure between regions. Compared to the observations, NICAM consistently has too many TTL clouds and too few low clouds. FV3 captures the mid-tropospheric cloud frequency but has too little cloud occurrence in the TTL in each region. ICON consistently has too many low clouds but not enough high clouds. In each region, ICON's cloud occurrence peaks in the upper troposphere at a much lower altitude than in the observations with convection rarely reaching the TTL. ICON looks marginally better in the SHL because it simulates more TTL clouds and the observed frequency is lower than over the ocean. In the TWP, SAM has a similar cloud occurrence to NICAM below ~ 11 km but does not have the same problem of simulating too many TTL clouds. None of the models clearly reproduce the cloud occurrence observed by CloudSat-CALIPSO from CCCM or by DARDAR in the ice-phase.

The legends in Figure 4.2a–c show the percent of clear-sky columns for each region. NICAM consistently has the fewest clear-sky columns followed by SAM, FV3, and ICON, respectively, for all regions. In the TWP, SAM captures the observed cloud cover most closely. There is more disagreement in the observations between DARDAR and CCCM in the SHL and NAU, so FV3 and SAM fall within the observed cloud cover range in both regions. ICON typically simulates too many clear-sky columns in the SHL and TWP but falls just within the range of observed cloud cover in NAU.

The vertical cloud occurrence is driven by the frequency and structure of convection in each model. The ice microphysics parameterizations may have a significant impact of the vertical structure of clouds, the TOA radiation budget, and the life cycle of cirrus.

4.3 FWP Categorization

The life cycle of ice clouds in the tropics is simplified into three main stages using the FWP. The FWP histograms for the TWP from Figure 3.3a–e are reproduced in Figure 4.3a–e as the green line. The FWP histograms for the SHL and NAU are in orange and purple respectively. The percent of columns in each category is listed above the histograms in each

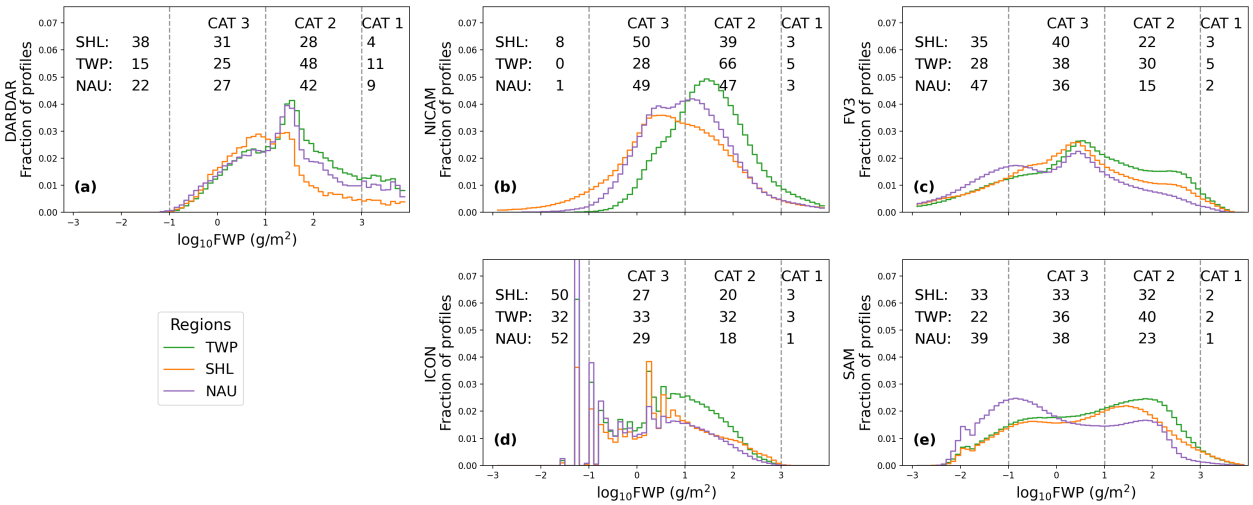

Figure 4.3: Normalized histograms of total column FWP for the SHL (orange), NAU (purple), and TWP histogram (green; same as black line in Figure 3.3 histograms) for (a) DARDAR, (b) NICAM, (c) FV3, (d) ICON, and (e) SAM. The categories are divided by vertical dashed lines. Columns with FWP below 0.1 g/m^2 are considered to be cirrus-free. Listed at the top of each subplot is the percent of columns from days 3–40 in each region for each category.

plot.

The oceanic regions have the highest observed occurrence of deep convection as measured by high FWP. DARDAR observations are from 2009 which had approximately 50% more precipitation in the TWP and NAU than 2016 in ERA-Interim reanalysis. Assuming all of this extra precipitation came from CAT 1, the lower bound on the expected CAT 1 frequency in 2016 is ∼7% (6%) in the TWP (NAU). Due to its larger footprint, CCCM only has a frequency of 2% (1%) for CAT 1 in the TWP (NAU). The observations provide a general guide for the range of values to compare with the models.

In the observations, the peaks in the FWP distributions all lie within CAT 2 but move towards larger FWPs from the SHL to NAU to TWP. The frequency of columns without ice clouds has the same trend: the SHL has the most ice-cloud-free columns (or least ice-cloud cover), followed by NAU and the TWP with progressively more cloud cover. NICAM and SAM capture the trend in the peak in FWP distribution, but only NICAM has the same

trend in ice-cloud frequency between regions. In NAU, FV3 and ICON each have fewer ice clouds, or more ice-cloud-free columns, and peak at smaller FWPs. In fact, all models have a bimodal peak in FWP distribution in NAU. Even though the bimodal distribution is not observed, it is possible that DARDAR's restrictive cloud mask algorithm filtered out some values of small FWP, especially when FWP is less than 10 g/m^2 (Cazenave et al., 2019), and eliminated the second peak.

NICAM and SAM tend to capture the key characteristics in FWP histograms between regions, but both models have consistent deficiencies across regions. NICAM does not simulate enough ice-cloud-free columns in any region. FV3 peaks at a FWP in CAT 3, much lower than in the other models or observations. ICON has a nearly normal distribution around 10 g/m^2, though noisy at smaller FWP values, and a low CAT 1 frequency. SAM tends to have very few columns in CAT 1 which may contribute to its inability to simulate columns with high albedo-low OLR values.

The behavior of ice microphysical parameterizations are partially revealed through the FWP histogram, we see that ICON tends to generate smaller ice masses than other models or observations, consistent with the joint albedo-OLR histogram showing few columns of deep convection whereas NICAM simulates lots of thick cirrus with FWP between 1 to 100 g/m^2 and has trouble generating ice-free columns. Nonetheless, dynamics and other sub-grid parameterizations may also play a role in the formation and maintenance of cirrus.

4.4 Life Cycle Proxy

Figure 4.4 uses the albedo-OLR plane as a proxy for the life cycle through the three main life stages given by the FWP CATs. Here, we zoom into different sections of the albedo-OLR plane so the x and y scales of each plot are different. Unlike Figure 4.1, the models are not coarsened to match CCCM in order to capitalize on the fine resolution of the GSRMs. The black line of neutral CRE is only drawn for the TWP region; the line for NAU is nearly identical but at much higher albedo in the SHL. There is generally more inter-model variability in CAT 1 than intra-model, or regional, variability. As we progress through the

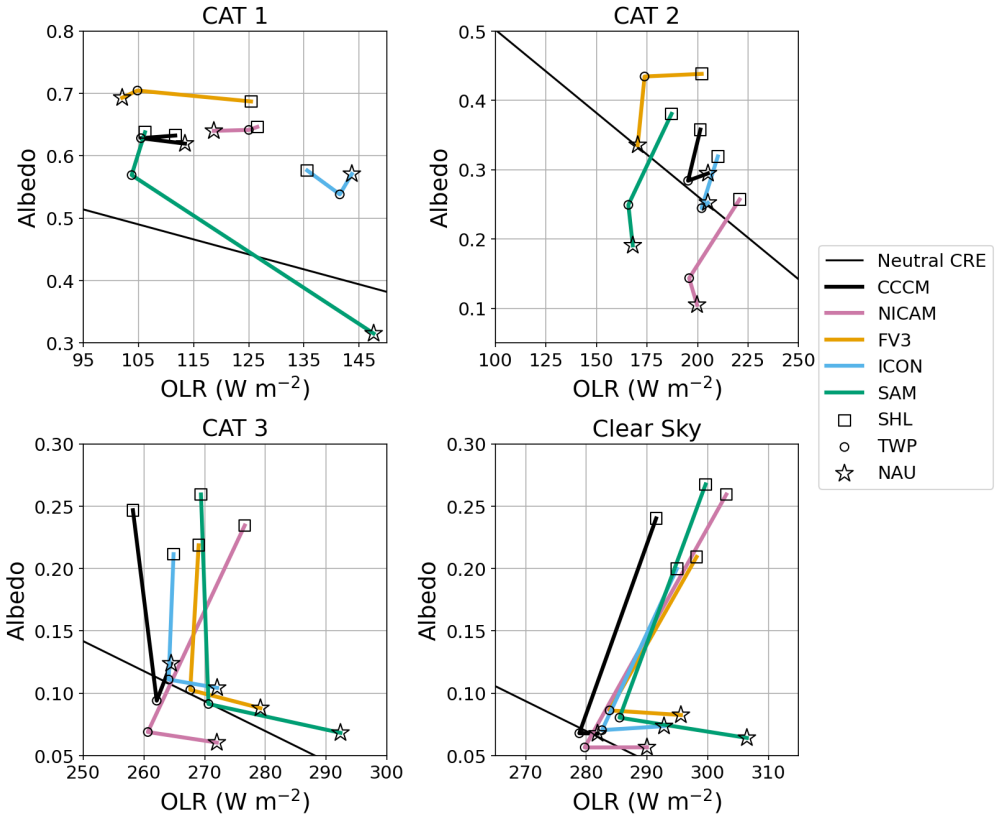

Figure 4.4: CAT median values for the SHL (square), TWP (circle), and NAU (star) in each model and CCCM. The scale and axis limits are different for CAT 1 and 2. Compared to Clear Sky, CAT 3 is shifted to lower OLR values by 15 W/m^2 but has the same x and y scales. The line of neutral CRE calculated from CCCM is shown for the TWP.

categories to clear sky, the opposite occurs with the models generally agreeing with each other in each region.

Aside from SAM, CAT 1 is clustered well within each model. The data suggests that tropical deep convection is similar across regions in both OLR and albedo. The models tend to have regional shifts in OLR rather than albedo, suggesting the optical thickness of CAT 1 remains consistent but the cloud-top heights differ, with disagreement on which region has the highest cloud tops. ICON has the SHL with the highest cloud top, but FV3 and NICAM have NAU. The observations and SAM agree that the TWP has a higher cloud top height

than the other regions.

In CAT 2, the models are still distinct and have large variation in albedo but relatively consistent OLR across regions. The models agree that the SHL has the highest median albedo. CAT 2 contains the largest range of cloud types including stratiform cloud decks, anvil outflow, thick cirrus, or a mixture of cloud types. The presence and albedo of liquid clouds beneath anvils and cirrus also greatly affect the CAT 2 albedo-OLR pairing, especially SAM which generates the most liquid clouds in CAT 2 of the models.

CAT 3 has clear regional differences independent of the chosen model. The bright surface of the SHL dominates the albedo value in Figure 4.4. The thin cirrus in ICON tend to have underlying liquid clouds over the ocean which alter the albedo significantly. Furthermore, the OLR values in the SHL and TWP are on par with each other for most models. This may be due to the cirrus occurring at similar altitudes within each model, only differing in the surface albedo.

The clear-sky median values are determined by the surface albedo and the water vapor profiles. Due to less convection bringing moisture to the upper troposphere, the SHL and NAU have less water vapor in the upper level causing the OLR to be higher than in the TWP region. The oceanic regions have the same clear-sky albedo and the SHL has a clear-sky albedo more than 0.1 higher. CAT 3 median values are shifted from the clear-sky values due to the presence of cirrus clouds. Thin cirrus over land have about double the LW warming effect than cirrus over the ocean. NICAM has the weakest warming effect from cirrus in the SHL but the strongest in the TWP. The other models are very similar with a LW CRE of $\sim$30 W/m^2 in the SHL and 15–20 W/m^2 in the TWP and NAU.

Chapter 5

TTL CIRRUS

Since we saw the strong effect of cirrus in CAT 3 on LW heating at TOA in Chapter 4.4, we investigate a particular subset of cirrus that may have a stronger LW heating, TTL cirrus. The TTL is the layer of the atmosphere that has properties of both the troposphere and stratosphere, approximately 14–18 km above sea level in the tropics. The high altitude of clouds in this layer may counteract the strong cooling effect of convection in the tropics.

5.1 Categorization

The TTL IWP was calculated by integrating the 3D cloud ice within the 14–18 km layer for FV3, ICON, and SAM. We calculated the total frozen condensate FWP in the TTL for DARDAR and NICAM because NICAM provides all frozen hydrometeors and DARDAR cannot differentiate the different hydrometeors. We expect the missing snow and graupel to affect CAT 1 values slightly, but there is likely not a significant impact on CAT 2 or 3. In Figure 5.1, the TTL IWP histogram for CAT 1 (green) is plotted on the bottom then the TTL IWP histogram for CAT 2 (red) is stacked on top of that with CAT 3 (blue) stacked on top of them both. The black line shows the histogram of the total TTL IWP. The time-mean frequency of columns in each category that contains TTL cirrus is listed in the legend. DARDAR has a near-native grid so we can directly compare to the models. The cloud threshold of 0.1 g/m^2 described in 2.4.1 for TTL IWP is also used here to determine the presence of a cloud in the TTL. Columns below this threshold are shaded in gray in the histogram because they do not constitute clouds in the TTL.

Despite how well NICAM's distribution matches the shape of observed TTL FWP in Figure 5.1ii, the histogram is shifted to larger IWPs than TTL FWP from DARDAR by

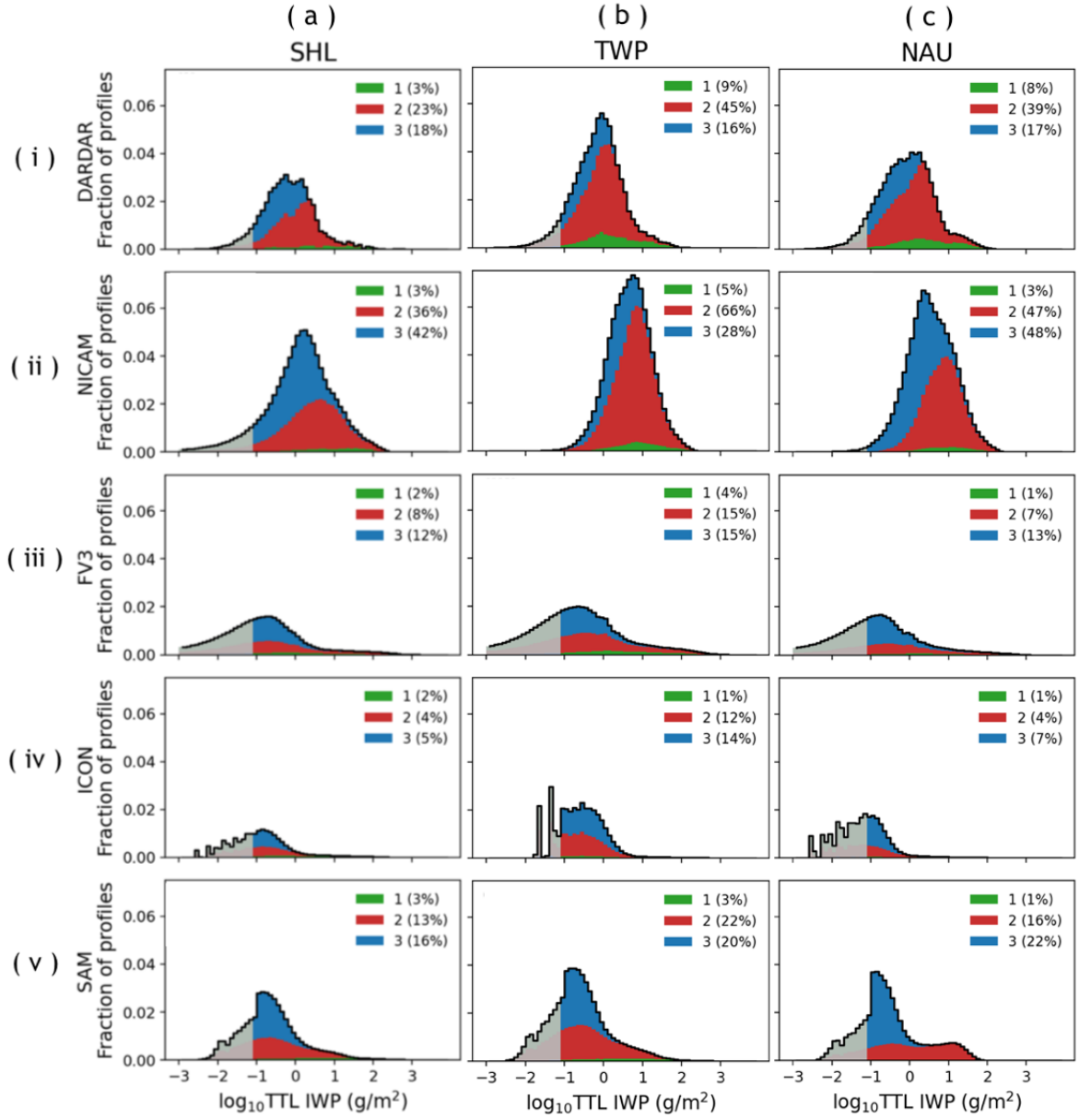

Figure 5.1: Stacked histogram of the TTL IWP (g/m^2) integrated from 14–18km for each total-column FWP category for the models and TTL FWP for DARDAR. CAT 1 (green) indicates the TTL IWP over deep convection; CAT 2 (red) is TTL cirrus above or connected to anvil and is stacked on top of CAT 1; CAT 3 (blue) is stacked on top of CAT 2. The black line is the total histogram of TTL FWP/IWP.

an order of magnitude. Only NICAM roughly captures the observed proportions of the categories in each region. FV3, ICON, and SAM all have roughly equal proportions of TTL cirrus in CATs 2 and 3 as quantified in the legends of Figure 5.1iii-v. The TTL IWP is smallest in ICON and rarely exceeds 5 g/m^2 in the TWP or 1 g/m^2 in the SHL and NAU. This is likely due to the lack of deep convection; since ICON has very few deep convective towers reaching the TTL, the ice that does manage to reach the TTL has a very small mass. FV3, ICON, and SAM tend to generate small values of ice in the TTL that cannot be defined as a cloud; however, these particles still interact with LW and SW radiation.

Ice over deep convection tends to have a larger mass than TTL ice outside of convection for each model even though CATs 2 and 3 have a higher frequency of occurrence. The area fraction of TTL cirrus is distributed much differently between models. These differences are large compared to the regional differences within a particular model.

5.2 Life cycle of TTL cirrus

In CAT 1, ice clouds in the TTL mean that TTL cirrus overlay a convective tower or deep convection has penetrated the TTL, bringing ice and moisture above the 14 km level. For CAT 2, ice clouds in the TTL may indicate thick TTL cirrus or TTL cirrus with underlying ice clouds, such as anvils or lower-altitude cirrus. CAT 3 typically has only one cloud layer that we would call thin cirrus; thus, if there is ice in the TTL, the cirrus cloud top occurs in the TTL, but the cloud base may be lower. The percent of columns with TTL cirrus are listed in Table 5.1 for the models and observations in each region.

Although CAT 2 has the most cirrus in the TTL in DARDAR and NICAM, CAT 1 has a larger percentage of ice in the TTL for all models (Table 5.1). This is consistent with the findings from Part I that nearly all of the mass flux of frozen water into the TTL is associated with deep convection. However, after convection dissipates, the cirrus persist over a larger area (CATs 2 and 3) than the original convective tower, suggesting that there is outflow from convective regions or hydration of the TTL.

ICON has much less TTL cirrus present in each CAT while NICAM has too much (Table

Table 5.1: Frequency of TTL cirrus for the Sahel, TWP and Nauru is shown for each category as a percent of columns in that category. The frequency of isolated TTL cirrus (i.e. clouds in the TTL but no clouds below the TTL) is shown as a percent of all columns.

	Sahel				TWP				Nauru			
	CAT 1	CAT 2	CAT 3	Iso TTL Ci	CAT 1	CAT 2	CAT 3	Iso TTL Ci	CAT 1	CAT 2	CAT 3	Iso TTL Ci
DARDAR	81	74	67	1	84	79	71	1	88	81	73	1
CCCM	71	32	8	3	88	49	22	6	66	24	8	2
NICAM	97	94	86	9	100	100	99	3	100	100	99	11
FV3	80	41	32	2	89	53	40	1	92	59	43	1
ICON	37	21	12	1	41	34	35	3	20	15	15	1
SAM	79	40	46	5	84	53	53	4	85	67	56	7

Note. Iso TTL ci = Isolated TTL cirrus.

5.1). Despite the large variations in cloud populations in the joint albedo-OLR histogram of SAM across regions, the frequency of TTL cirrus in each CAT in SAM falls within the range of observed frequencies. The frequency of TTL cirrus in FV3 is high for CAT 1 likely due to the strong convection in FV3. CATs 2 and 3 in FV3 are well within the observed range for each region.

5.3 Isolated TTL Cirrus

Optically thin, high-altitude clouds such as isolated TTL cirrus should have the largest greenhouse warming effect because LW warming outweighs the SW cooling. The CRE is has the strongest warming for cirrus with FWP in the range of 20–60 g/m^2 and then decreases as FWP increases. Around 200 g/m^2, the SW CRE strengthens enough to neutralize the LW warming at TOA. Eventually, the SW cooling dominates with large FWPs (Berry & Mace, 2014).

Table 5.1 includes the frequency of isolated TTL cirrus for the observations and models in each region, for which we calculated the LW, SW, and Net CRE and plotted in Figure 5.2. The cloud mask used for DARDAR, which aims to reduce the noise in the data as much as possible, inevitably excludes some thin or isolated cirrus layers. Consequently, DARDAR underestimates the amount of isolated cirrus (Cazenave et al., 2019). While CCCM has a

much coarser horizontal resolution, limiting its ability to observe thin cirrus, it also uses a less restrictive cloud mask than DARDAR. Thus, CCCM has a higher frequency of isolated TTL cirrus than DARDAR in Table 5.1. Aside from NICAM and SAM in both the SHL and NAU, the models fall within the range of observations from DARDAR to CCCM. NICAM and SAM in the SHL and NAU overestimate the amount of isolated TTL cirrus.

Figure 5.2 shows the LW, SW, and net CRE for each region and model. A positive CRE denotes warming, and vice versa. Each model tends to agree more over the ocean than land in both LW and SW CRE. The oceanic regions show slight warming because the SW CRE is so small that the LW CRE dominates. Since isolated TTL cirrus are so thin, they have a very small net CRE. The presence of TTL cirrus in a column has a LW CRE anywhere from 1 to 17 W/m^2 in oceanic regions (Figure 5.2). Due in part to uncertainty as well as variance in surface albedo, all models have the SW CRE as positive in the SHL. This uncertainty in CRE calculations of ± 5 W/m^2, due to the estimated clear-sky albedo and, to a lesser extent, the OLR. Thus, the positive values of SW CRE in the SHL are real output from the model, suggesting the models have more reflective TTL cirrus over land.

The models simulate isolated TTL cirrus with different ice microphysics. The average IWP in the TTL for columns with isolated TTL cirrus differs between the models. Averaged across all regions, FV3, ICON, and SAM are reasonably close to each other with 0.27 g/m^2, 0.43 g/m^2, and 0.51 g/m^2, respectively, but NICAM has a mean IWP an order of magnitude larger, at 3.4 g/m^2. NICAM does have a stronger LW CRE than the other models in the TWP, but not in the SHL or NAU.

As shown in Figure 5.2, the data from CCCM shows warming in all three regions from isolated TTL cirrus. The warming effect of isolated TTL cirrus is strongest in the SHL. We do not coarsen the model data here because isolated TTL cirrus occur on such small scales that spatial averaging may lose significance; instead, we consider the data to be a rough guideline and do not expect the models to reproduce the observed values exactly. The warming effect is much stronger in the SHL than in the oceanic regions. The models overemphasize this regional difference. The models show the strongest cooling in the TWP,

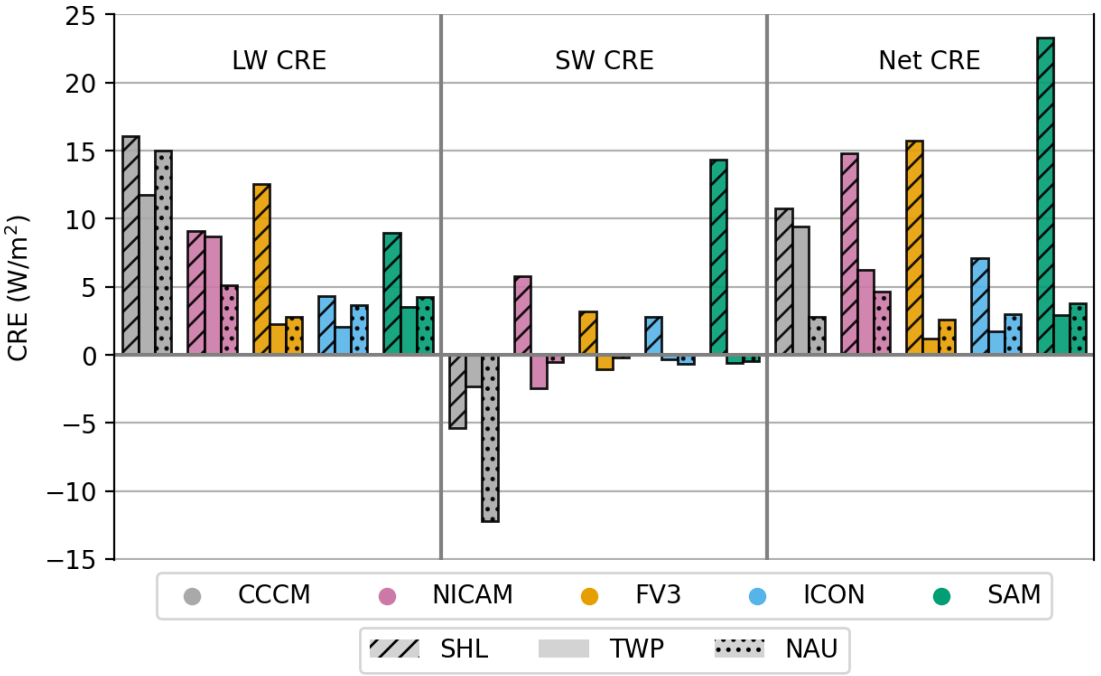

Figure 5.2: Isolated TTL Cirrus CRE for each model including LW (left), SW (center), and Net (right) CRE for SHL (striped), TWP (solid) and NAU (dotted). The CRE values are plotted with positive (negative) values indicating warming (cooling).

contrary to the data. The net CRE ends up being too small in the TWP. In NAU, the model output of LW and SW CRE is much less than the data, but these differences cancel out in the net CRE, all having around 4 W/m^2 (Figure 5.2).

The models show isolated TTL cirrus have a net warming effect, from 1 W/m^2 in the TWP for FV3 to over 20 W/m^2 in the SHL for SAM.

The effects of isolated TTL cirrus emphasize the impact of cirrus in the TTL on LW warming at TOA. The large differences between models seen in sections 3 and 4 are greatly diminished in the TTL, especially with isolated TTL cirrus and their radiative impacts.

Chapter 6

SUMMARY AND CONCLUSIONS

The life cycle of tropical clouds has typically been determined from observations. Here, we analyze the life cycle in GSRMs and provide a comparison between the DYAMOND models and satellite observations. GSRMs provide grid resolutions that are fine enough to simulate a reasonable life cycle as a product of the explicitly resolved convection. We use a statistical approach to examine the life cycle of modeled convective systems in the DYAMOND GSRMs. Three $10^\circ \times 10^\circ$ latitude-longitude regions in the tropics are used to represent convection in the tropics: two regions with ocean convection (TWP and NAU) and one with land convection (SHL).

The aggregate life cycle of tropical cirrus begins with convective systems then transitions to anvils and, finally, thin cirrus with correspondingly smaller FWPs. After convective injection, each model simulates a path to thin cirrus in the albedo-OLR plane. The fact that these paths are different indicate inherent model differences in microphysics and fine scale dynamics.

Each model tends to have a characteristic climatology, but each still qualitatively captures regional differences. NICAM has a low mean OLR from its excessive TTL cirrus extent but reasonably reproduces the observed cloud populations and captures the regional differences quite well. FV3 has the least radiative biases in the 40-day climatology, but produces too many low clouds. FV3 also simulates deep convection well in all three regions, but does not capture some key observed differences between regions. ICON consistently fails to simulate deep convection at high albedo-low OLR values. The low cloud fraction and weak convection lead to the low OLR variance seen in the model biases. ICON tends to have little change in the characteristic cloud populations between regions. Nonetheless, the simulated life cycles

in ICON through the albedo-OLR plane are closest to the observed life cycle in each region. SAM does not simulate sufficiently thick convective cores and instead tends to generate thick anvil clouds marked by low albedo values.

The life cycles in the models scatter around the observed life cycle path in the albedo-OLR plane. Deep convection has larger differences between models than between regions, but as the clouds thin and spread the differences between models reduce, and there is a clear difference between the land and ocean regions. The transition from deep convection to thin cirrus is largely determined by the cloud structure below the TTL and types of clouds most common in each model.

Our results support previous findings that the overall warming effect of thin cirrus, though small, may contribute significantly to reducing the strong cooling effect of deep convection in the TWP (e.g., Berry & Mace, 2014). The presence of TTL cirrus tends to strengthen the warming effect of anvils or reduce the cooling effect of low clouds. However, there are rarely instances of isolated TTL cirrus, so the warming effect is small compared to columns with accompanying clouds below the TTL. The clouds between deep convection and thin cirrus such as anvils, stratiform cirrus clouds, and low clouds have a significant impact on the CRE. These clouds, especially in CAT 2, also have the largest inter-model differences due to the variety of cloud types present.

One motivation for using GSRMs is to expand our understanding of tropical cirrus by filling in observational gaps, but the models need further improvements to be more useful for studying the physical properties of the TTL and the life cycle of tropical clouds. Improvements for each model could include changes to the model physics, such as improved ice microphysics. In addition, analysis would be enhanced by saving model variables such as full 3D frozen hydrometeor output for radiatively active hydrometeors and optical depth to directly compare radiative effects to observations. Nonetheless, GSRMs in the DYAMOND simulations provide an illuminating range of model behavior and simulated TTL cirrus which will only be enhanced by further improvements in model sub-grid processes.

6.1 Future Work

Sensitivity studies would help determine how microphysics parameterizations affect the presence and radiative effects of TTL cirrus. Future work could include the role of cirrus in dehydrating the TTL in GSRMs. Simulations of boreal winter from DYAMOND2, the second phase of the DYAMOND project, may also provide an interesting contrast to the summer simulations presented here. Both DYAMOND sets of GSRMs provide ample opportunity for studying the TTL, its properties, and cirrus clouds.

REFERENCES

Ackerman, T., Liou, K.-N., Valero, F., & Pfister, L. (1988). Heating rates in tropical anvils. *J. Atmos. Sci.*, *45*(10), 1606-1623. Retrieved from https://doi.org/10.1175/1520-0469(1988)045\%3C1606:HRITA\%3E2.0.CO;2

Berry, E., & Mace, G. G. (2014). Cloud properties and radiative effects of the asian summer monsoon derived from a-train data. *Journal of Geophysical Research: Atmospheres*, *119*(15), 9492-9508. Retrieved from https://agupubs.onlinelibrary.wiley.com/doi/abs/10.1002/2014JD021458 doi: https://doi.org/10.1002/2014JD021458

Brewer, A. (1949). Evidence for a world circulation provided by the measurements of helium and water vapor distribution in the stratosphere. *Q. J. R. Meteorol. Soc.*, *75*, 351-363. Retrieved from https://doi.org/10.1002/qj.49707532603 doi: 10.1002/qj.49707532603

Cazenave, Q., Ceccaldi, M., Delanoë, J., Pelon, J., Groß, S., & Heymsfield, A. (2019). Evolution of dardar-cloud ice cloud retrievals: new parameters and impacts on the retrieved microphysical properties. *Atmospheric Measurement Techniques*, *12*(5), 2819–2835. Retrieved from https://www.atmos-meas-tech.net/12/2819/2019/ doi: 10.5194/amt-12-2819-2019

Delanoë, J., & Hogan, R. J. (2008). A variational scheme for retrieving ice cloud properties from combined radar, lidar, and infrared radiometer. *Journal of Geophysical Research: Atmospheres*, *113*(D7). Retrieved from https://agupubs.onlinelibrary.wiley.com/doi/abs/10.1029/2007JD009000 doi: https://doi.org/10.1029/2007JD009000

Delanoë, J., & Hogan, R. J. (2010). Combined cloudsat-calipso-modis retrievals of the properties of ice clouds. *Journal of Geophysical Research: Atmospheres*, *115*(D4). Retrieved from https://agupubs.onlinelibrary.wiley.com/doi/abs/

10.1029/2009JD012346 doi: https://doi.org/10.1029/2009JD012346

Del Genio, A. (2012). Representing the sensitivity of convective cloud systems to tropospheric humidity in general circulation models. *Surv Geophys*, *33*, 637–656. Retrieved from https://doi.org/10.1007/s10712-011-9148-9 doi: 10.1007/s10712-011-9148-9

Deng, M., Mace, G. G., Wang, Z., & Lawson, R. P. (2013, 04). Evaluation of Several A-Train Ice Cloud Retrieval Products with In Situ Measurements Collected during the SPARTICUS Campaign. *Journal of Applied Meteorology and Climatology*, *52*(4), 1014-1030. Retrieved from https://doi.org/10.1175/JAMC-D-12-054.1 doi: 10.1175/JAMC-D-12-054.1

Dessler, A., Ye, H., Wang, T., Schoeberl, M., Oman, L., Douglass, A., ... Portmann, R. (2016). Transport of ice into the stratosphere and the humidification of the stratosphere over the 21st century. *Geophysical Research Letters*, *43*(5), 2323-2329. Retrieved from https://agupubs.onlinelibrary.wiley.com/doi/abs/10.1002/2016GL067991 doi: https://doi.org/10.1002/2016GL067991

Dinh, T., Fueglistaler, S., Durran, D., & Ackerman, T. (2014). Cirrus and water vapour transport in the tropical tropopause layer – part 2: Roles of ice nucleation and sedimentation, cloud dynamics, and moisture conditions. *Atmospheric Chemistry and Physics*, *14*(22), 12225–12236. Retrieved from https://acp.copernicus.org/articles/14/12225/2014/ doi: 10.5194/acp-14-12225-2014

Doelling, D. R., Sun, M., Nguyen, L. T., Nordeen, M. L., Haney, C. O., Keyes, D. F. ., & Mlynczak, P. E. (2016a, 03). Advances in Geostationary-Derived Longwave Fluxes for the CERES Synoptic (SYN1deg) Product. *Journal of Atmospheric and Oceanic Technology*, *33*(3), 503-521. Retrieved from https://doi.org/10.1175/JTECH-D-15-0147.1 doi: 10.1175/JTECH-D-15-0147.1

Doelling, D. R., Sun, M., Nguyen, L. T., Nordeen, M. L., Haney, C. O., Keyes, D. F., & Mlynczak, P. E. (2016b, 03). Advances in Geostationary-Derived Longwave Fluxes for the CERES Synoptic (SYN1deg) Product. *Journal of Atmospheric and Oceanic Technology*, *33*(3), 503-521. Retrieved from https://doi.org/10.1175/JTECH-D-15

-0147.1 doi: 10.1175/JTECH-D-15-0147.1

Fueglistaler, S., Dessler, A. E., Dunkerton, T. J., Folkins, I., Fu, Q., & Mote, P. W. (2009). Tropical tropopause layer. *Rev. Geophys.*, *47*(RG1004). Retrieved from doi.org/10.1029/2008RG000267 doi: 10.1029/2008RG000267

Gasparini, B., Blossey, P. N., Hartmann, D. L., Lin, G., & Fan, J. (2019). What drives the life cycle of tropical anvil clouds? *Journal of Advances in Modeling Earth Systems*, *11*(8), 2586-2605. Retrieved from https://agupubs.onlinelibrary.wiley.com/doi/abs/10.1029/2019MS001736 doi: https://doi.org/10.1029/2019MS001736

Hartmann, D. L., & Berry, S. E. (2017). The balanced radiative effect of tropical anvil clouds. *Journal of Geophysical Research: Atmospheres*, *122*(9), 5003-5020. Retrieved from https://agupubs.onlinelibrary.wiley.com/doi/abs/10.1002/2017JD026460 doi: https://doi.org/10.1002/2017JD026460

Hartmann, D. L., Moy, L. A., & Fu, Q. (2001). Tropical convection and the energy balance at the top of the atmosphere. *Journal of Climate*, *14*, 4495-4511.

Hartmann, D. L., & Short, D. A. (1980, 06). On the Use of Earth Radiation Budget Statistics for Studies of Clouds and Climate. *Journal of the Atmospheric Sciences*, *37*(6), 1233-1250. Retrieved from https://doi.org/10.1175/1520-0469(1980)037<1233:OTUOER>2.0.CO;2 doi: 10.1175/1520-0469(1980)037⟨1233:OTUOER⟩2.0.CO;2

Highwood, E., & Hoskins, B. (1998a). The tropical tropopause. *Quarterly Journal of the Royal Meteorological Society*, *124*(549), 1579-1604. Retrieved from https://doi.org/10.1002/qj.49712454911 doi: 10.1002/qj.49712454911

Hollars, S., Fu, Q., Comstock, J., & Ackerman, T. (2004). Comparison of cloud-top height retrievals from ground-based 35 ghz mmcr and gms-5 satellite observations at arm twp manus site. *Atmospheric Research*, *72*(1), 169-186. Retrieved from https://www.sciencedirect.com/science/article/pii/S0169809504000717 (Clouds and Radiation) doi: https://doi.org/10.1016/j.atmosres.2004.03.015

Houze, R. A. (1981). Cloud clusters in large-scale vertical motions in the tropics. *Journal of the Meteorological Society of Japan*, *60*(1), 396-410. Retrieved from https://doi.org/

10.2151/jmsj1965.60.1_396 doi: 10.2151/jmsj1965.60.1_396

Houze, R. A., & Betts, A. (1981). Convection in gate. *Rev. Geophys.*, *19*, 541-576.

Inoue, T., Satoh, M., Hagihara, Y., Miura, H., & Schmetz, J. (2010). Comparison of high-level clouds represented in a global cloud system–resolving model with calipso/cloudsat and geostationary satellite observations. *Journal of Geophysical Research: Atmospheres*, *115*(D4). Retrieved from https://agupubs.onlinelibrary.wiley.com/doi/abs/10.1029/2009JD012371 doi: https://doi.org/10.1029/2009JD012371

Jensen, E., & Pfister, L. (2004). Transport and freeze-drying in the tropical tropopause layer. *Journal of Geophysical Research: Atmospheres*, *109*(D2). Retrieved from https://agupubs.onlinelibrary.wiley.com/doi/abs/10.1029/2003JD004022 doi: https://doi.org/10.1029/2003JD004022

Jensen, E., Pfister, L., Jordan, D. E., Bui, T. V., Ueyama, R., Singh, H. B., ... Pfeilsticker, K. (2017). The nasa airborne tropical tropopause experiment: High-altitude aircraft measurements in the tropical western pacific. *Bulletin of the American Meteorological Society*, *98*(1), 129 - 143. Retrieved from https://journals.ametsoc.org/view/journals/bams/98/1/bams-d-14-00263.1.xml doi: 10.1175/BAMS-D-14-00263.1

Johnson, R. H., Rickenbach, T. M., Rutledge, S. A., Ciesielski, P. E., & Schubert, W. H. (1999, 08). Trimodal Characteristics of Tropical Convection. *Journal of Climate*, *12*(8), 2397-2418. Retrieved from https://doi.org/10.1175/1520-0442(1999)012<2397:TCOTC>2.0.CO;2 doi: 10.1175/1520-0442(1999)012⟨2397:TCOTC⟩2.0.CO;2

Kato, S., Rose, F. G., Rutan, D. A., Thorsen, T. J., Loeb, N. G., Doelling, D. R., ... Ham, S.-H. (2018, 05). Surface Irradiances of Edition 4.0 Clouds and the Earth's Radiant Energy System (CERES) Energy Balanced and Filled (EBAF) Data Product. *Journal of Climate*, *31*(11), 4501-4527. Retrieved from https://doi.org/10.1175/JCLI-D-17-0523.1 doi: 10.1175/JCLI-D-17-0523.1

Kato, S., Rose, F. G., Sun-Mack, S., Miller, W. F., Chen, Y., Rutan, D. A., ... Collins, W. D. (2011). Improvements of top-of-atmosphere and surface irradiance computations with calipso-, cloudsat-, and modis-derived cloud and aerosol properties. *Journal*

of Geophysical Research: Atmospheres, *116*(D19). Retrieved from https://agupubs.onlinelibrary.wiley.com/doi/abs/10.1029/2011JD016050 doi: https://doi.org/10.1029/2011JD016050

Kiehl, J. T. (1994). On the observed near cancellation between longwave and shortwave cloud forcing in tropical regions. *Journal of Climate*, *7*(4), 559-565. doi: 10.1175/1520-0442(1994)007⟨0559:OTONCB⟩2.0.CO;2

Liu, C., & Zipser, E. J. (2005). Global distribution of convection penetrating the tropical tropopause. *Journal of Geophysical Research*, *110*(D23), D23104. Retrieved 2020-10-25, from http://doi.wiley.com/10.1029/2005JD006063 doi: 10.1029/2005JD006063

Long, C. N., Mather, J. H., & Ackerman, T. P. (2016, 06). The ARM Tropical Western Pacific (TWP) Sites. *Meteorological Monographs*, *57*, 7.1-7.14. Retrieved from https://doi.org/10.1175/AMSMONOGRAPHS-D-15-0024.1 doi: 10.1175/AMSMONOGRAPHS-D-15-0024.1

Mace, G. G., Deng, M., Soden, B., & Zipser, E. (2006). Association of tropical cirrus in the 10–15-km layer with deep convective sources: An observational study combining millimeter radar data and satellite-derived trajectories. *Journal of the Atmospheric Sciences*, *63*(2), 480 - 503. Retrieved from https://journals.ametsoc.org/view/journals/atsc/63/2/jas3627.1.xml doi: 10.1175/JAS3627.1

Nugent, J., Turbeville, S., Bretherton, C., Ackerman, T., & Blossey, P. (2021). Tbd. *TBD*.

Ramanathan, V., Cess, R. D., Harrison, E. F., Minnis, P., Barkstrom, B. R., Ahmad, E., & Hartmann, D. (1989). Cloud-radiative forcing and climate: Results from the earth radiation budget experiment. *Science*, *243*(4887), 57–63. Retrieved from https://science.sciencemag.org/content/243/4887/57 doi: 10.1126/science.243.4887.57

Sassen, K., Wang, Z., & Liu, D. (2009). Cirrus clouds and deep convection in the tropics: Insights from calipso and cloudsat. *Journal of Geophysical Research: Atmospheres*, *114*(D4). Retrieved from https://agupubs.onlinelibrary.wiley.com/doi/abs/10.1029/2009JD011916 doi: https://doi.org/10.1029/2009JD011916

Sokol, A., & Hartmann, D. (2018). Tropical anvil clouds: Radiative driving towards a preferred state. *JGR: Atmospheres*.

Stephens, G. L. (2005). Cloud feedbacks in the climate system: A critical review. *Journal of Climate*, *18*(2), 237-273. Retrieved from https://journals.ametsoc.org/view/journals/clim/18/2/jcli-3243.1.xml doi: 10.1175/JCLI-3243.1

Stephens, G. L., Vane, D. G., Boain, R. J., Mace, G. G., Sassen, K., Wang, Z., ... Team, C. S. (2002). The cloudsat mission and the a-train: A new dimension of space-based observations of clouds and precipitation. *Bull. Amer. Meteorol. Soc.*, *83*, 1771–1790. doi: 10.1175/BAMS-83-12-1771

Stevens, B., Satoh, M., Auger, L., Biercamp, J., Bretherton, C. S., Chen, X., ... Zhou, L. (2019). DYAMOND: the DYnamics of the Atmospheric general circulation Modeled On Non-hydrostatic Domains. *Prog Earth Planet Sci*, *6*(61), 895-918. Retrieved from https://doi.org/10.1186/s40645-019-0304-z doi: 10.1186/s40645-019-0304-z

Virts, K. S., & Houze, R. A. (2015). Clouds and water vapor in the tropical tropopause transition layer over mesoscale convective systems. *Journal of the Atmospheric Sciences*, *72*(12), 4739 - 4753. Retrieved from https://journals.ametsoc.org/view/journals/atsc/72/12/jas-d-15-0122.1.xml doi: 10.1175/JAS-D-15-0122.1

Virts, K. S., Wallace, J. M., Fu, Q., & Ackerman, T. P. (2010, 10). Tropical Tropopause Transition Layer Cirrus as Represented by CALIPSO Lidar Observations. *Journal of the Atmospheric Sciences*, *67*(10), 3113-3129. Retrieved from https://doi.org/10.1175/2010JAS3412.1 doi: 10.1175/2010JAS3412.1

Yoneyama, K., Zhang, C., & Long, C. N. (2013). Tracking pulses of the madden–julian oscillation. *Bulletin of the American Meteorological Society*, *94*(12), 1871 - 1891. Retrieved from https://journals.ametsoc.org/view/journals/bams/94/12/bams-d-12-00157.1.xml doi: 10.1175/BAMS-D-12-00157.1